


12-2011

## Spectroscopic studies of melamine at high pressure

Martin Donald Galley  
*University of Nevada, Las Vegas*

Follow this and additional works at: <https://digitalscholarship.unlv.edu/thesesdissertations>

 Part of the [Biological and Chemical Physics Commons](#), [Condensed Matter Physics Commons](#), and the [Optics Commons](#)

---

### Repository Citation

Galley, Martin Donald, "Spectroscopic studies of melamine at high pressure" (2011). *UNLV Theses, Dissertations, Professional Papers, and Capstones*. 1385.  
<https://digitalscholarship.unlv.edu/thesesdissertations/1385>

This Thesis is protected by copyright and/or related rights. It has been brought to you by Digital Scholarship@UNLV with permission from the rights-holder(s). You are free to use this Thesis in any way that is permitted by the copyright and related rights legislation that applies to your use. For other uses you need to obtain permission from the rights-holder(s) directly, unless additional rights are indicated by a Creative Commons license in the record and/or on the work itself.

This Thesis has been accepted for inclusion in UNLV Theses, Dissertations, Professional Papers, and Capstones by an authorized administrator of Digital Scholarship@UNLV. For more information, please contact [digitalscholarship@unlv.edu](mailto:digitalscholarship@unlv.edu).

SPECTROSCOPIC STUDIES OF MELAMINE AT HIGH PRESSURE

By

Martin Donald Galley

A thesis submitted in partial fulfillment  
of the requirements for the

Master of Science in Physics

Department of Physics and Astronomy  
College of Sciences  
The Graduate College

University of Nevada, Las Vegas  
December 2011



## **Thesis Approval**

The Graduate College  
The University of Nevada, Las Vegas

November 7, 2011

This thesis prepared by

**Martin Donald Galley**

entitled

**Spectroscopic Studies of Melamine at High Pressure**

is approved in partial fulfillment of the requirements for the degree of

**Master of Science in Physics**

Department of Physics

Michael Pravica, Committee Chair

Andrew Cornelius, Committee Member

Stephen Lepp, Committee Member

Clemens Heske, Graduate College Representative

Ronald Smith, Ph. D., Vice President for Research and Graduate Studies and Dean of the Graduate College

## ABSTRACT

### Spectroscopic Studies of Melamine at High Pressure

By

Martin D. Galley

Dr. Michael Pravica, Examination Committee Chair

Professor of Physics

University of Nevada, Las Vegas

We have performed mid- and far- Infra Red (IR) absorption, Raman spectroscopy, and angular dispersive x-ray diffraction (XRD) studies on melamine under high pressure and room temperature. We have verified the presence of two prior reported phase transitions, the first between 1 - 2 GPa, and the second between 7 - 9 GPa. We have also found evidence of a third unreported phase transition between 14 - 16 GPa, during which, there was a sudden disappearance of all low energy peaks ( $<500\text{ cm}^{-1}$ ) in both the Raman and IR spectra. The far-IR peak movement experiences a discontinuity as the rate of peak movement suddenly changes. The XRD pattern shows a dramatic change in crystal structure between 11 and 16 GPa. We observed softening of the N-H symmetric and anti-symmetric vibrations with pressure, suggesting that intermolecular hydrogen bonding increases as the intermolecular distance decreases similarly to what was observed in TATB [20]. The molecular decomposition data from core intramolecular peaks of mid IR and Raman show complete reversibility, giving evidence that the melamine did not chemically decompose at high pressures. Melamine merits this investigation into its high pressure behavior as it has many similarities with some high explosives. The closest cousin to melamine is the secondary explosive TATB, which is in the same symmetry group  $D_{3h}$  [16]. Understanding the exact science of explosives is

an extremely difficult process, therefore approaching the problem from the examination of a similar inert compound may help yield a better understanding of explosives and the novel routes to the synthesis of ultra-hard materials such as  $C_3N_4$

## Acknowledgements

I would like to thank my advisor Dr. Michael Pravica for giving me the freedom to forge my own path through research while still guiding me through many other important lessons and experiences. Your shared wisdom and advice will be with me for the rest of my life.

Dr. Clemens Heske taught me a great majority of what I know about group theory, synchrotrons, and spectroscopic theory. Thank you for your outstanding classes and lessons.

Thank you to the rest of my committee, Dr. Stephen Lepp and Dr. Andrew Cornelius, for listening and critiquing my long presentations and thesis paper.

My family has always been there to support and guide me through the good and difficult times of college and life. I could never have gotten this far without their love and help. Thank you

My co-workers and colleagues Jason Baker, Daniel Antonio, Brad Clarke, Michael Haire, John Howard, Ed Romano, John Robinson, and Yu Liu you made the good times great and the bad times bearable. The bond formed from working with you on the long assignments and take home tests or late nights at the labs will not easily be forgotten.

My many friends who I've made at the National Labs, some have helped me greatly through my Graduate experience. Nenad Velisavljevic from Los Alamos, thank you for your help in working with the x-ray diffraction patterns and the professional lessons you taught me about performing great research. Zhenxian Liu at Brookhaven, your guidance and wisdom were essential for the IR studies. The HP CAT team at Argonne, especially Changyong Park, and Curtis Kenny-Benson for all their help in taking the XRD patterns.

The physics department staff and professors, you taught me just how much more I had and still have to learn, you challenged me academically and made me a better scientist because of it, I can't thank you enough.

To all my friends, my family, and my God, without you I would be nothing. I am eternally indebted to you all, thank you.

## TABLE OF CONTENTS

ABSTRACT.....	iii
ACKNOWLEDGMENTS.....	v
LIST OF FIGURES.....	vii
CHAPTER 1	
INTRODUCTION.....	1
CHAPTER 2	
EXPERIMENTAL TECHNIQUES AND COMPUTATIONAL METHODS	
Light Sources: Lasers.....	2
Light Sources: Synchrotrons.....	5
X-Ray Diffraction.....	6
Ruby Measurements.....	8
Raman Microscope.....	10
Peak Analysis.....	12
Vibrational Spectroscopy.....	13
Fourier Transformed Infrared Spectroscopy (FTIR).....	14
Raman Spectroscopy.....	15
Group Theory.....	18
Infrared Spectroscopy Experimental Setup.....	19
Raman Spectroscopy Experimental Setup.....	23
X-Ray Diffraction Setup.....	24
CHAPTER 3	
RESULTS AND DISCUSSION	
Low Wavenumber.....	25
Mid Range Wavenumber.....	30
High Wavenumber Studies in the 2800-3600 cm <sup>-1</sup> Range.....	37
X-Ray Diffraction.....	40
Decompression.....	43
CHAPTER 4	
CONCLUSION.....	47
APPENDIX.....	49
REFERENCES.....	50
VITA.....	52

## LIST OF FIGURES

Figure 1	Structural Model of Melamine and TATB.....	1
Figure 2	Cavity Resonance Modes and Gain Bandwidth.....	3
Figure 3	Double Crystal Monochromator schematic.....	7
Figure 4	Ruby Electronic Structure.....	9
Figure 5	Ruby Pressure Offset.....	10
Figure 6	Raman Schematic.....	11
Figure 7	Layout of Interferometer.....	22
Figure 8	Stacked Plot of Far-IR.....	26
Figure 9	Low Wavenumber Raman Spectra Stacked Plot.....	26
Figure 10	IR Peak Movement 100-300 $\text{cm}^{-1}$ .....	27
Figure 11	IR Peak Movement 380-685 $\text{cm}^{-1}$ .....	28
Figure 12	Raman Peak Position 100-450 $\text{cm}^{-1}$ .....	28
Figure 13	Raman Peak Position of C-N bonds.....	29
Figure 14	Vibrational Schematic of Modes A.....	33
Figure 15	Vibrational Schematic of Modes B.....	33
Figure 16	Vibrational Schematic of Modes C.....	33
Figure 17	Mid-IR Stacked Plot.....	35
Figure 18	IR Peak Position of C-N bonds.....	36
Figure 19	Mid Range Wavenumber Stacked Plot.....	36
Figure 20	Raman Peak Position of C-N Bonds.....	37
Figure 21	High Wavenumber Raman Stacked Plot.....	38
Figure 22	IR Peak Positions of $\text{NH}_2$ Bonds.....	39
Figure 23	Raman Peak Positions of N-H Bonds.....	39
Figure 24	X-ray Diffraction of Pressures 0-5GPa.....	41
Figure 25	X-Ray Diffraction of Pressures 5-9 GPa.....	42
Figure 26	X-Ray Diffraction of High Pressure Phase Transition.....	43
Figure 27	Raman Decompression for Low Wavenumber.....	44
Figure 28	Decompression X-Ray Diffraction Patterns.....	44
Figure 29	IR Decompression of C-N Vibrations.....	45
Figure 30	IR Decompression of N-H Vibrations.....	46
Figure 31	Raman Decompression for High Wavenumbers.....	46
Figure 32	Raman Decompression for Mid Range Wavenumbers.....	47



CHAPTER 1  
INTRODUCTION

Melamine ( $C_3N_6H_6$ ) is an industrially synthesized chemical which is often found in household dishware. When treated with different chemicals such as Formaldehyde, it works as an excellent fire retardant [1]. Even without treatment, melamine will not combust or even burn very well, yet, it has a very similar structure to a well known explosive, TATB, which, like melamine is in the  $D_{3h}$  symmetry group. Such a disparity between the two compound's behavior raises questions as to why one is an explosive (TATB) whereas the other is a fire retardant (melamine). Melamine has an s-triazine ring of alternating carbon and nitrogen atoms with three amino branches. As depicted in Figure 1:

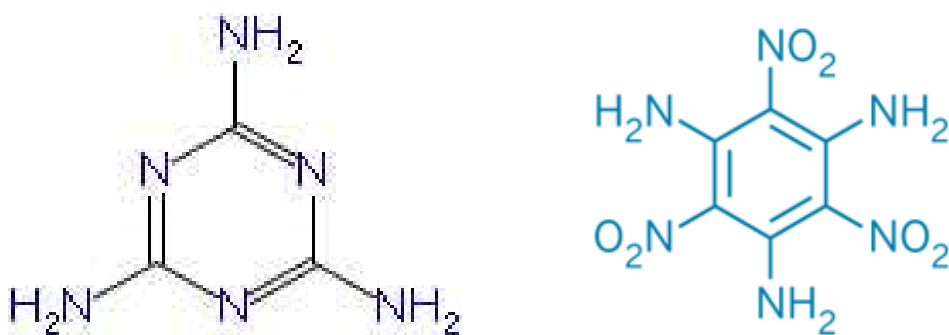


Figure 1: Structural model of melamine (left) [2] and TATB (right) [3]

The amine branches' high nitrogen content have enabled melamine to be detected as a faux protein which, being toxic, resulted in the recent tainted milk epidemic in China where melamine was added to infant milk as a cheap protein additive [4]. Melamine may under high pressure and temperature, become an ultra hard-carbon nitride  $C_3N_4$  with a

bulk modulus greater than diamond [5]. With all these questions, understanding the behavior of melamine under extreme conditions will be very helpful to the scientific community. To the best of our knowledge, we present in this thesis the first far-IR study of melamine at high pressures and the highest pressure IR study of melamine to date.

## CHAPTER 2

### EXPERIMENTAL TECHNIQUES AND COMPUTATIONAL METHODS

#### Light Sources: Lasers

To perform the Raman spectroscopy experiment, a high intensity monochromatic narrow bandwidth light source is required. An argon ion laser was used because of a laser's spectrally narrow beam profile and high intensity. The beam profile and narrowness is determined by a multitude of factors and equations. Within the resonating chamber (the cavity) of a laser there are a certain number of modes ( $\nu$ ) available based on [7]:

$$\Delta\nu = \frac{c}{2l}$$

where  $l$  is the length of the cavity and  $c$  is the speed of light in a vacuum (as an example the red peaks in Figure 2 are separated by a distance  $\frac{c}{2l}$ ). As a rule of thumb, the longer the cavity, the fewer the modes, and the greater the separation of the modes. The mirrors on each side of the cavity are not perfectly parallel so there are other modes (or multiple wavelengths) that resonate. This results in several modes that simultaneously resonate and a wide range of lasing wavelengths (roughly 70 nm wide), which is not spectrally narrow enough to perform Raman spectroscopy. To narrow the beam profile, a prism is placed inside the cavity to disperse all the wavelengths of light that are not wanted and

allow only one wavelength to pass straight through the prism and be amplified in the cavity [6].

There is a delicate balance between the laser intensity and spectral bandwidth. The greater the gain, the more modes that fit within the gain bandwidth line which implies that there will be a greater range of unwanted emitted wavelengths (the right image in Figure 2 can help visualize this).

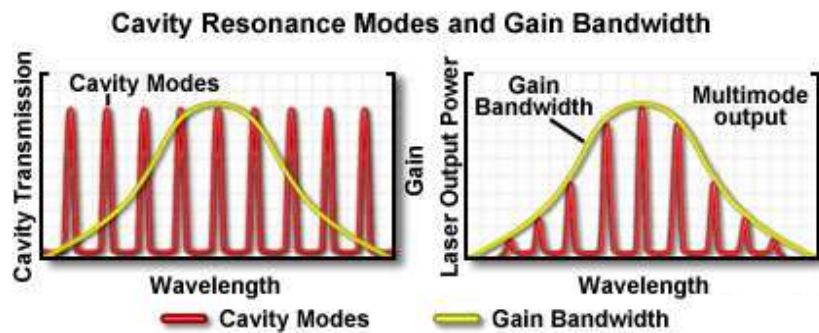


Figure 2: The red lines are the modes present in a cavity, while the yellow line is the line function or the gain bandwidth. When both components of the power equation combine they make the red line on the right image. The mode intensity fits inside the line function envelope [31].

Lowering the gain implies lowering the number of excited atoms in the population inversion and decrease the intensity. The width of the frequency distribution (i.e. the line function), is most dependent on the temperature, gain medium, and function of population inversion. These equations and concepts of laser power are a summarization of the notes taken in a laser theory course taught by Professor Victor Kwong at UNLV and from the book *Quantum Electronics* by Yariv Amnon. The right image in Figure 2 is the compilation of two equations which are derived from the following equation [7]:

$$P_0(\nu) = \frac{2P_0 l T_1 \mathcal{L}(\nu)}{(1 - Re^{\bar{\alpha} l})^2} \left[ \frac{1}{1 + \frac{4Re^{\bar{\alpha} l} \sin^2(\beta \nu) l}{(1 - Re^{\bar{\alpha} l})^2}} \right]$$

$P_0$  is the power,  $l$  is the cavity length,  $T_1$  is the transmission through the exiting mirror,  $\mathcal{L}(\nu)$  is the line function which forms the shape of the gain bandwidth,  $R$  is the reflection coefficient of the two mirrors,  $\bar{\alpha}$  is the gain coefficient, and  $\beta$  is the phase shift length. The equation can be broken down into two parts  $A(\nu)$  and  $T(\nu)$ .  $A(\nu)$  represents the frequency mode envelope or gain bandwidth in Figure 2 and is described by the line function and reflectivity of the two mirrors as seen in the following equation. To simplify the equation, it is easiest to assume that the active medium has been removed ( $\alpha = 0$ ):

$$A(\nu) = \left[ \frac{\mathcal{L}(\nu)}{(1 - R)^2} \right]$$

$T(\nu)$  represents the mode frequency and width, as can be seen in the next equation.

$$T(\nu) = \frac{1}{1 + \frac{4R}{(1 - R)^2} \sin^2(\beta l)}$$

The red lines labeled “cavity modes” on the left image of Figure 2 are  $T(\nu)$ .

With the gain bandwidth sufficiently narrow, the gain adequately high, and the modes separated, an etalon can be placed inside the resonating chamber to further alter the effective length of the cavity to fit a single mode. This will create a narrow Gaussian distribution of the beam profile, however, there are edge effects that could result in other wavelengths lasing with enough intensity to alter the Raman spectra. A spatial filter placed after the laser is a quick solution to knock out the edge effects not corrected by the laser apparatus. This results in a very smooth and narrow Gaussian distribution of the

beam profile, centered around the desired wavelength. One can now be confident of a minimal error in the chosen wavelength, which makes this laser a good choice for performing Raman spectroscopy.

The intensity is also important when detecting Raman shifts, because, out of roughly every  $10^6$  photons, only one or two will experience an inelastic collision and be detected. This could lead to very long acquisition times for a low intensity laser.

### Light Sources: Synchrotrons

Synchrotrons proved to be vital in many of these experiments as they can provide high photon intensity as well as wide energy ranges. The High Pressure- Collaborative Access Team (HP-CAT) of Sector 16 in Advanced Photon Source (APS) at Argonne National Laboratory (ANL) and the U2A infrared beamline in the National Synchrotron Light Source (NSLS) at Brookhaven National Laboratory (BNL) were the two synchrotron facilities used for the x-ray diffraction (XRD) and infrared (IR) studies respectively. Infrared experiments require a wide range of frequencies to interact with the sample in order to determine which energies excite bond vibrations; whereas angular dispersive x-ray diffraction experiments requires a highly monochromatic light source. NSLS utilizes a bending magnet to create the broad bandwidth of light whereas at APS we use an undulator. Light is created as an electron is accelerated, so bend magnets accelerate the particles around a curve to produce light. The critical wavelength of light( $\lambda_c$ ) created by the bending magnet is determined by the radius (R) of the light curve divided by  $\gamma$  ( $\gamma = \frac{E}{mc^2}$ ) [8]:

$$\lambda_c = \frac{4}{3} \frac{\pi R}{\gamma^3}$$

The electron energy throughout the storage ring is kept constant. The curve's radius was designed so that the critical wavelength of the bend magnet produces light in the infrared region.

An undulator (insertion device) works in a similar fashion to bending magnets; the critical difference is that instead of a single bend, the electron beam is forced onto an undulating path down a straight section. The electron oscillates quickly enough that its wave function overlaps with the photon wave packet emitted in earlier bends causing a coherent superposition of emitted radiation. These create narrow frequency pulses of x-rays with very high intensities proportional to  $N^2$  where  $N$  is the number of undulations [8]. The photon count per second produced in a bending magnet is roughly  $10^{13}$  while in an undulator, the count is  $10^{15}$ , decreasing experiment times by a factor of 100 [8]. X-ray diffraction experiments require monochromatic light but normal optical gratings are not applicable to hard x-rays. To create monochromatic light, a silicon crystal monochromator is used. Hard x-ray beamlines create filtered radiation using two crystals via x-ray diffraction, by taking advantage of the Bragg equation to pass only the wavelengths desired. They are known as Kirkpatrick-Baez (KB) mirrors.

### X-ray Diffraction

The atoms in a crystal are arranged in one of only seven lattice systems [9]. These structures are determined by the lengths of three primitive translation vectors  $a$ ,  $b$ , and  $c$  as well as the angles between them  $\alpha$ ,  $\beta$ , and  $\gamma$ . These parameters can be arranged to form cubic, trigonal, hexagonal, tetragonal, orthorhombic, monoclinic, and triclinic systems [9]. Each of these systems contains lattices which form a unique set of lattice planes inside the crystal structure. An incident photon of light can elastically scatter off

the electron cloud surrounding each atom to constructively interfere and form a plane wave, provided the inter-atomic distance is a multiple of the wavelength of incident light.

Using Bragg's equation:

$$n\lambda = 2d\sin\theta$$

one can utilize the angle of the diffracted light along with a constant wavelength of light to determine the inter-atomic distances. When  $\sin\theta = \frac{n\lambda}{2d}$  there is an obvious spike in the photon count which implies that a lattice plane is present at that angle satisfying the diffraction condition. Once the peaks are determined to be at certain angles, one can decipher the crystal structure. X-rays are high energy photons that can penetrate into the bulk of a material where the lattice structure is relatively constant. Most materials have an inter-atomic distance on the order of a few angstroms which requires the wavelength of light to be of the same order.

A double crystal monochromator uses this principle by changing the angle of the crystal ( $\theta$ ) to filter a specific wavelength. The rotated crystal diffracts the desired wavelength out at an angle of  $2\theta$ , whereas the second crystal catches this beam and redirects the beam back toward its original incident direction (see Figure 3).

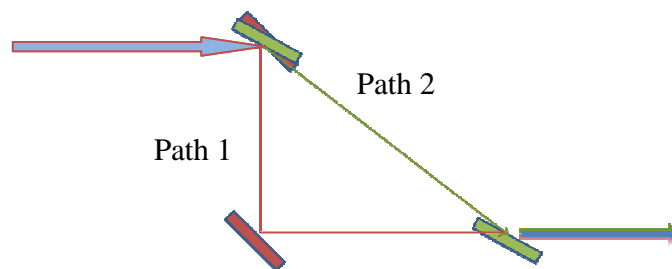


Figure 3: A double crystal monochromator with two different angles to show how different angles capture different wavelengths.

As a structural phase transition is approached via increasing pressure, the crystal structure will begin to re-arrange itself to lower its free energy. This will cause the diffraction peaks to simplify if the new phase represents a less complicated lattice system with more symmetry (such as an orthorhombic structure transitioning into a cubic). If the lattice converts to a more complicated phase, less symmetric crystal system, the diffraction peaks might split and new peaks may appear where there were none previously. This is due to new lattice planes forming due to the more structurally complicated lattice. By observing XRD spectra with pressure, we gather evidence for phase transitions.

#### Ruby Measurements

Ruby has two fluorescence peaks which are well documented and used to determine pressure in both hydrostatic and non-hydrostatic conditions. The  $R_1$  line generally has a wavelength of 694.25 nm at atmospheric pressure [10]. As pressure is increased, there is a decrease in the energy level separation. This decrease in energy is noted as an increasing wavelength that is commonly used for determining the pressure inside a diamond anvil cell (among other methods). Figure 4 shows the electronic structure of ruby and illustrates that the electrons jump to the  ${}^4T_1$  and the  ${}^4T_2$  band when excited before decaying via vibrational energy to the  ${}^2E$  band, which is metastable [10]. The electrons further decay to the ground state by emitting a photon which is detected by a spectrometer.



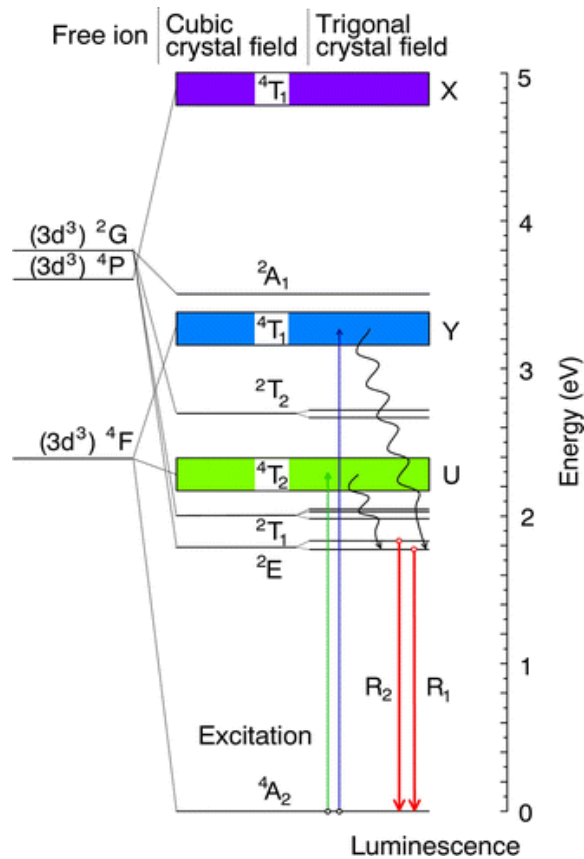


Figure 4: Ruby Electronic Structure [10]

The ruby pressure versus wavelength curve was originally calibrated with pressure using the equation of state (EOS) of NaCl [11]. This was experimentally tested up to 20 GPa with a high degree of accuracy. Upon increasing pressures to greater than 20 GPa, the accuracy begins to deviate from the linearity of the NaCl EOS [11]. Therefore, the fluorescence wavelength has been mapped to follow the following equation  $P$  (Mbar) =  $(19.04/5) \{[(\lambda_0 + \Delta\lambda)/\lambda_0]^5 - 1\}$ , where  $\lambda_0$  is the atmospheric pressure wavelength of ruby [11]. This achieves a high degree of accuracy up to 100 GPa and was calibrated with specific volume measurements of four different metals under pressure. The maximum uncertainty at 100 GPa is slightly greater than 1%, while below 20 GPa the percent error is around 0.1% [11]. The plots in Figure 5 are two ruby spectra taken during the Raman

experiment, which demonstrates the change in the peak position with pressure and spectra linewidth broadening.

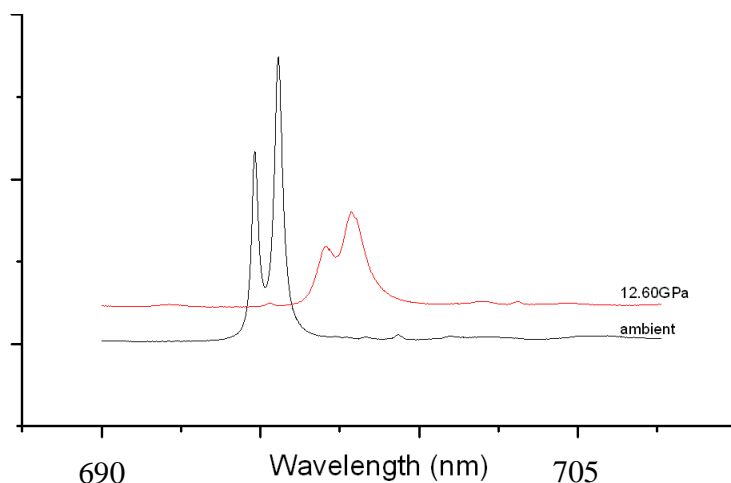


Figure 5: Two ruby spectra taken at different pressures.

### Raman Microscope

Raman spectroscopy was performed using a Spectra-Physics BeamLok® argon ion laser tuned to 514.5 nm as the excitation source. The laser was set to 35 mW for the experiments, to increase the signal to noise ratio, as opposed to the typical power output of 5 mW. Unwanted laser heating was not an issue as melamine does not experience any change in its structure up to 600°C and diamonds are excellent conductors of heat [2]. The laser beam would enter a Nikon MM-40 Measuring Microscope, pass through and reflect from a beam splitter and enter a 20x objective onto the sample. A higher power objective was not used due to spatial restrictions associated with the size of the DAC. The objective would collect scattered light, pass it back through the beam splitter and out the exit port of the microscope and enter to the Horiba Jobin-Yvon Triax 550®

monochromator. Before entering the monochromator, the light would pass through a double convex lens with a focal length of 45 mm. The laser beam diameter at the lens is 2mm which yields an f-number of ( $f\# = 22.5$ ) within the f-number of the monochromator ( $f\#=6.4$ ), but at a poor resolution. The Raman setup is shown in Figure 6.

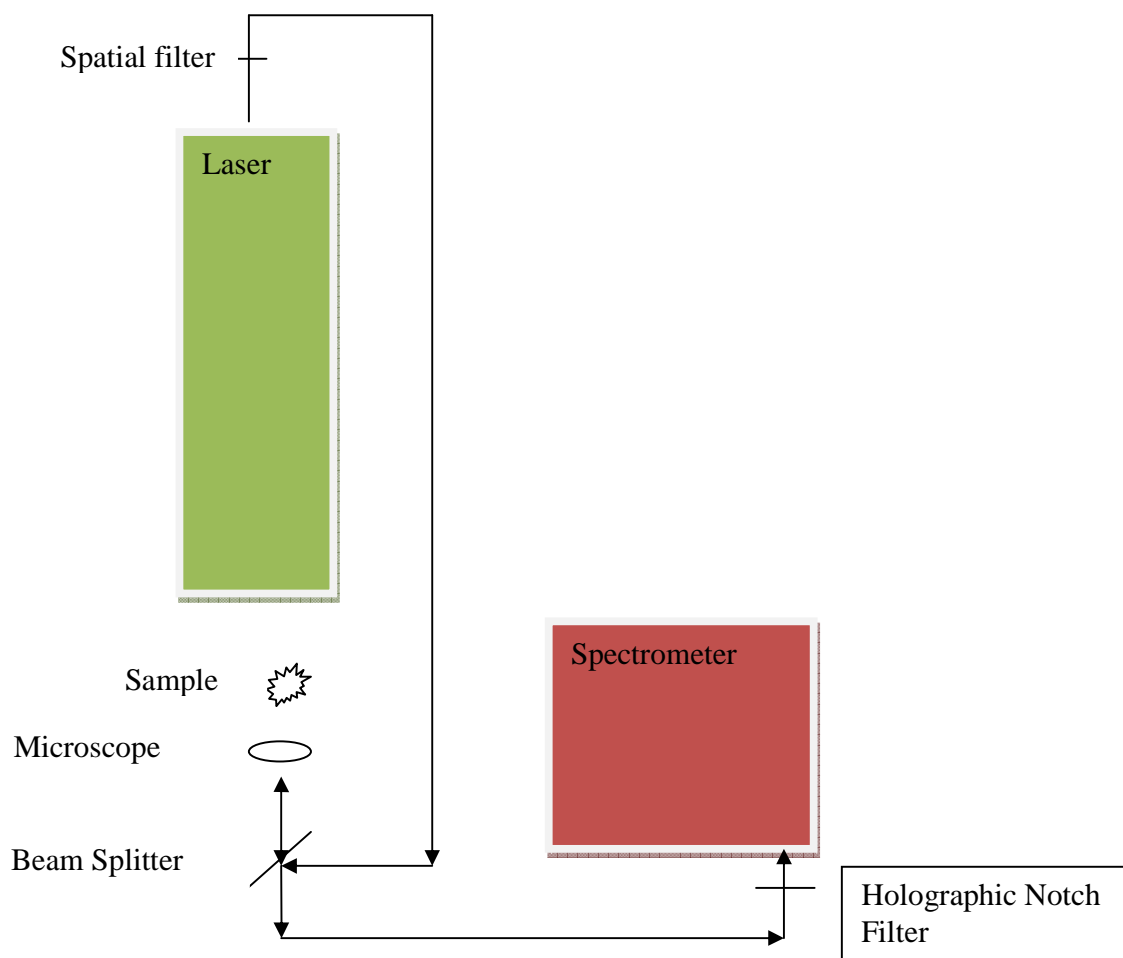


Figure 6: Raman schematic measuring system [13]

The detector we used was a Princeton Instruments liquid nitrogen cooled Spec 10 CCD® (Charge Coupled Device), which was the photon counter. The liquid nitrogen reservoir maintained the CCD temperature at  $-120^{\circ}\text{C}$  for the experiments. The CCD is

1340 pixels wide and must be manually calibrated for wavelength position using a spectral lamp. The monochromator grating has 1200 lines/mm which yields a range of  $\sim 1200 \text{ cm}^{-1}$ . We used four wavelengths to calibrate our investigated range ( 534 nm, 565 nm, 615 nm, and 700 nm). This was accomplished using a UVP neon pen-lamp, which has multiple emission lines at each of the chosen spectral ranges. The emission lines used for each range are written in table 1.

Spectrometer Wavelength (nm)

<u>534nm</u>	<u>565nm</u>	<u>615nm</u>	<u>700nm</u>
520.39	574.83	607.43	692.95
533.08	576.44	609.62	702.41
534.11	580.45	612.85	703.24
540.06	582.02	614.31	717.39

Table 1: Spectrometer wavelength and emission lines frequencies used in calibration.

Our calibrations were performed once and checked intermittently to determine the reproducibility of the monochromator driver. The error of reproducibility was within  $\frac{1}{100}$  of a wavenumber. This is within the spectrometer resolution of  $1.02 \text{ cm}^{-1}$  per pixel.

Peak Analysis

To determine the peak center, the PeakFit® program was used. The peak type chosen was generally a Voigt profile, which is a combination of Gaussian and Lorentzian profiles [14]. This hybrid profile is chosen due to two different effects that broaden the peak center. A Gaussian profile is created by the velocity distribution of particles in the

sample as well as the active medium within the laser [7]. The Lorentzian profile is caused by the Heisenberg uncertainty principle, more specifically the time it takes for photon emission [7]. If the time it takes for the excited atom to emit is  $\tau = \Delta t$  then the uncertainty is  $\Delta E = \frac{\hbar}{\tau}$ . The dependence on wavelength with respect to energy is  $\Delta\lambda = \frac{\hbar c}{\Delta E}$ , which is the natural line width as well as the Lorentzian profile [7]. The signal to noise ratio for the Raman spectra was high for these data points and were consequently smoothed using a Fast Fourier Transform. This requires the data to be Fourier transformed, truncated, and then reverse transformed. This operates under the idea that the spectral noise is of a higher frequency than the spectral bands within the transform domain [15]. The truncation removes high frequency data and ultimately lowers the signal to noise ratio. The error in the fitted peak centroid was determined as a standard error reported by the PeakFit® software.

### Vibrational Spectroscopy

Infrared spectroscopy detects the transitions between vibrational and rotational modes of molecules [16]. For the experiments on melamine, the rotational modes can be mostly ignored because melamine is in solid state at room temperature, thus frustrating the translational and rotational movement of the molecules. Assuming that the vibrations are small allows the potential energy of the molecular bonds to be approximated as though it is a simple harmonic oscillator. The frequency is calculated to be a function of the force constant ( $k$ ) and the reduced mass of the atoms ( $\mu$ ) [16]:

$$\nu = \frac{1}{2\pi} \sqrt{\frac{k}{\mu}}$$

(For these experiments the pressure will be increased which will result in a decrease of intermolecular distance, causing an increase in the coulombic forces and ultimately the force constant, via anharmonic interactions. Therefore, for our experiment we expect the frequency of our vibrations to increase with pressure.) A quantum harmonic oscillator is known to possess a function of the frequency  $\nu$  and have discrete energies separated by a vibrational quantum number  $v$  as follows [16]:

$$E_v = h\nu \left( v + \frac{1}{2} \right)$$

The only electric dipole allowed transitions between vibrational energies occur when  $\Delta v = \pm 1$ . The abscissa and ordinate values are generally reported in IR and Raman to be the intensity versus the wavenumber. A wavenumber denoted as  $\tilde{\nu}$ , has the units of  $\frac{1}{cm}$ , and is related to the frequency by

$$\tilde{\nu} = \frac{\nu}{c}$$

The wavenumber is a relative wavenumber that is chosen with respect to the incident laser wavelength:

$$\tilde{\nu} = \frac{\nu_0 - \nu_f}{c}$$

where  $\nu_0$  is the frequency of the incoming laser light and  $\nu_f$  is the frequency of the scattered light.

### Fourier Transformed Infrared (*FTIR*) Spectroscopy

To be infrared active (i.e. observed), certain selection rules must be met. Most importantly, the electric dipole moment of the molecule must change when it vibrates [17]. The emitted photon is classically thought of as the electromagnetic field interacting with the molecules oscillating electric dipole causing it to absorb the incident photon and

vibrate. This only requires the dipole moment to change; there need not be a permanent dipole either before or after the transition takes place [17]. More on the selection rules will be covered in the group theory section discussed later.

Infrared spectroscopy can be performed by studying only a small range of energies at a time with a monochromator. Using a Fourier Transform spectrometer enables several frequencies or wavenumbers to be examined simultaneously without a loss in data and requires a polychromatic source. The FTIR method uses an Michelson interferometer to produce an interferogram which provides a quick way of analyzing a wide range of wavenumbers in what is called the multiplex advantage [18]. The interferogram pattern exists in its frequency domain and while in that state, the data displays the power density variation as a function of the difference in path-length. To translate from the frequency dimensions to space dimensions a Fourier Transform pair is used in [18]:

$$I(\delta) = \int_0^{\infty} B(\tilde{\nu}) \cos 2\pi\tilde{\nu}\delta \, d\tilde{\nu}$$

$$B(\delta) = \int_0^{\infty} I(\tilde{\nu}) \cos 2\pi\tilde{\nu}\delta \, d\delta$$

The second equation shows a variation of intensity as a function of difference in path length [18], this is the form all of the IR data is presented in.

### Raman Spectroscopy

Raman spectroscopy is a vibrational transition detection method very similar to infrared. Both methods work complementary towards one another, due to the differences in which they stimulate and detect the vibrational transitions. In Raman scattering, a photon is temporarily absorbed by a molecule which temporarily places it into to a forbidden

virtual excited state. When the molecule returns to its ground state, it must discharge the extra energy as a photon again. The vast majority of the time that photon is emitted with the same energy it was absorbed with, via elastic scattering or Rayleigh Scattering. On a rare occasion (about 1 in  $10^6$ ) the photon inelastically scatters, resulting in the molecule going to an excited vibrational state obeying the  $\Delta v = \pm 1$  selection rule, where  $v$  is the vibrational quantum number [18]. The emitted photon will have more or less energy than it arrived with, depending on if the molecule was already in the excited vibrational state or in the vibrational ground state respectively. If the outgoing photon has more energy than it arrived with, this is known as Anti-Stokes scattering and if there is less energy than initially, it is Stokes scattering [16&17]. The Boltzmann distribution shows that a significant majority of molecules will be in the ground vibrational state at ambient temperatures, so the number of molecules which would be excited is larger than the number of molecules which will be de-excited. Thus, the Stokes scattering has a stronger intensity than Anti-Stokes.

A very well detailed description of the theoretical background of Raman scattering is given in *Introductory Raman Spectroscopy* by John Ferraro. In the following, the key aspects are summarized, as taken from Ferraro [15]. A Raman active mode changes its polarizability as it vibrates whereas an IR active mode changes its dipole moment with vibrations. A well known condition that helps determine if a mode is Raman or IR active is the mutual exclusion principle. If a vibration is symmetric with a center of symmetry, then the mode is Raman active but not IR active, however; if the vibration is antisymmetric with respect to the center of symmetry, the mode is IR active but not Raman active.



Determining if the polarization changes in a vibrational mode can be determined by examining what happens when a laser is directed at a molecule. The intense incident photons from a laser produce a strong electromagnetic field that excites the vibrational modes and is given by

$$E = E_0 \cos 2\pi \nu_0 t$$

and produces a dipole moment:

$$\vec{P} = \vec{\alpha} \cdot \vec{E} = \vec{\alpha} \vec{E}_0 \cos 2\pi \nu_0 t$$

Where P and E are vectors in the x, y, and z direction and  $\vec{\alpha}$  is the polarizability tensor, this can be rewritten as

$$\begin{bmatrix} P_x \\ P_y \\ P_z \end{bmatrix} = \begin{bmatrix} \alpha_{xx} & \alpha_{xy} & \alpha_{xz} \\ \alpha_{yx} & \alpha_{yy} & \alpha_{yz} \\ \alpha_{zx} & \alpha_{zy} & \alpha_{zz} \end{bmatrix} \begin{bmatrix} E_x \\ E_y \\ E_z \end{bmatrix}$$

The polarizability tensor is symmetric because of the assumption that the energy is stored as potential energy i.e.;  $\alpha_{xy} = \alpha_{yx}$ ,  $\alpha_{xz} = \alpha_{zx}$ , and  $\alpha_{yz} = \alpha_{zy}$ . When one of the tensor values change under the influence of an oscillating electric field, the polarization changes as a result and the vibration mode is considered Raman active. Let us assume that the molecule vibrates with frequency  $\nu_m$ , then the nuclear displacement is

$$q = q_0 \cos 2\pi \nu_m t$$

Assume a small amplitude of vibration and thus the polarizability tensor can be linearized as a function of q

$$\alpha = \alpha_0 + \left( \frac{\partial \alpha}{\partial q} \right) q_0 + \dots$$

In this case  $\alpha_0$  represents its equilibrium polarizability and  $\left(\frac{\partial\alpha}{\partial q}\right)$  is the rate of change of the polarizability. When the equations are combined, we obtain:

$$P = \alpha_0 E_0 \cos 2\pi \nu_0 t + \frac{1}{2} (\partial\alpha/\partial q)_0 q_0 E_0 [\cos\{2\pi(\nu_0 + \nu_m)t\} + \cos\{2\pi(\nu_0 - \nu_m)t\}]$$

Here, the  $\nu_0$  is the elastically scattered light frequency called the Rayleigh scattering frequency, and  $\nu_m$  is the inelastically scattered light frequency or the Raman scattering frequency. The terms  $(\nu_0 + \nu_m)$  and  $(\nu_0 - \nu_m)$  refer to Stokes and Anti-Stokes frequencies respectively. If there is no change in the polarization then  $\left(\frac{\partial\alpha}{\partial q}\right)$  is zero and the mode is considered to be Raman inactive.

### Group Theory

Determining whether a mode will be RF active, IR active, or not active at all is most easily determined with group theory. A mathematical group always contains a well defined set of symmetry operations that must satisfy four group axioms; the axioms include closure, associativity, an identity, and an inverse [16]. In the group theory for molecules, there are five operation/elements used to separate the different molecular symmetries into groups. The identity, rotation, reflection, inversion, and the improper rotation will categorize each molecular arrangement into a symmetry group which all share certain traits brought about by their symmetry [16]. For example, based solely on their symmetry, H<sub>2</sub>O and SO<sub>2</sub> both belong in the C<sub>2v</sub> symmetry point group and both are non-polar and parallel to their principal axis. Using the point group to determine which modes are IR and Raman active requires a character table [16]. A detailed description of developing a character table can be found in *Physical Chemistry* by Peter Atkins and de Paula and is summarized in the following paragraph [16].

Developing a character table for a specific group first requires a matrix representative of all of the operations that make up that group, e.g.  $D(\sigma_v)$  for a vertical plane mirror operation. Next, a set of matrices which represent all the group operations are placed into matrix representation  $\Gamma$ . A matrix representation should be reduced and diagonalized until it cannot be further reduced; that representation is then referred to as an irreducible representation. All of the irreducible representations are placed into a character table and the molecular orbitals can be assigned to specific irreducible representations (irreducible. rep.). Each irreducible rep. is a type of possible vibrational mode on a molecule. If that mode is IR active, the orbital must be a linear orbital x, y, and z. A Raman active mode must have quadratic orbitals assigned to the mode such as  $x^2$ ,  $y^2$ ,  $z^2$ ,  $xy$ ,  $yz$  ...etc. Melamine is in the  $D_{3h}$  point group and possesses the following character table [16]:

**Character table for  $D_{3h}$  point group**

	E	$2C_3$	$3C'_2$	$\sigma_h$	$2S_3$	$3\sigma_v$	linear, rotations	quadratic
$A'_1$	1	1	1	1	1	1		$x^2+y^2, z^2$
$A'_2$	1	1	-1	1	1	-1	$R_z$	
$E'$	2	-1	0	2	-1	0	(x, y)	$(x^2-y^2, xy)$
$A''_1$	1	1	1	-1	-1	-1		
$A''_2$	1	1	-1	-1	-1	1	z	
$E''$	2	-1	0	-2	1	0	$(R_x, R_y)$	$(xz, yz)$

Table 2: The  $E'$  and  $A''_2$  irreducible representations have infrared active modes while the  $A'_1$ ,  $E'$ , and  $E''$  have Raman active modes [19].

### Infrared Spectroscopy Experimental Setup

Two separate IR experiments were performed on melamine in the far IR and mid-IR ranges. Both experiments used the same symmetric-style Diamond Anvil Cell (DAC)

with the same type of gasket (stainless steel, grade 304 or 316). The melamine used was of spectroscopic quality (>99.9%) from Alfa Aesar® and was from two different “batches” of melamine.

For each experiment, the gasket was prepared in the same manner by pre-indenting a stainless steel gasket (~250 µm thickness) and then drilling a sample chamber with an Electric Discharge Machine (EDM). The diamond culet was roughly 300 µm in diameter and the same IR quality, low fluorescence, type II diamonds were used for both experiments. For the mid-IR experiment, the gasket was pre-indented to ~50 µm in thickness with a sample chamber initial diameter of 120 µm. For the far-IR experiment, the gasket was pre-indented to a thickness of 22 µm and had a sample chamber diameter of 150 µm.

The sample preparation for each experiment diverges at this point due to the differing individual requirements for each experiment. In the mid-IR experiment, a Bruker Hyperion Vertex 80v® microscope was used with a 20x30 µm IR beam size. Potassium bromide (KBr) was used as a pressure transmitting medium as it is nearly transparent in the infrared spectrum. KBr powder was placed inside the sample chamber and then lightly pressed by the diamonds to ensure that it was tightly packed in the gasket. The gasket was temporarily removed and the diamonds were cleaned to prepare them for the sample. To prevent a near complete absorption of the IR transmission, a very thin amount of sample needed to be in the sample chamber. The sample was placed directly on the culet of one diamond and both diamond halves were brought together to crush the sample between them to roughly a 5 µm thickness. Excess sample was then cleared from ~ ½ of the diamond face to enable the background acquisitions. A test

acquisition was performed to ensure that there was a sufficient amount of sample to collect data with reasonable signal to noise but not too much to block the transmission signal. Once the sample thickness was deemed satisfactory, a thermally-relieved ruby sphere was placed inside the sample chamber to determine pressure and the DAC was closed and sealed. After each pressure increase, a new background spectrum was taken by manually translating the DAC on the microscope stage so that the acquisition zone was solely over the blank  $\frac{1}{2}$  of the sample chamber. This background was then automatically subtracted away from the sample pattern.

For the far-IR experiment, a larger sample diameter was required ( $\sim 100 \mu\text{m}$ ), as the far IR wavelengths are typically of the same order. As far-IR is utilized for its ability to detect intermolecular interactions, an amorphous substance with little or no far-IR signature is needed. Petroleum jelly was used as the pressure transmitting medium for our experiment which is transparent to far-IR wavelengths. The diamond halves were first brought together and touching without the sample and a background spectrum was acquired. This background spectrum was subtracted from all of the collected sample spectra. No further background spectra were taken as changes in background due to the increases in pressure or the change in path length produce no noticeable changes to the spectra of petroleum jelly. Then, melamine powder was placed over the entire diamond culet to ensure a maximum signal to noise. Lastly, a thermally relieved ruby sphere was placed inside the sample chamber and then the entire assembly was sealed by manually translating the diamonds to deform the gasket and sample enclosed. The far-IR detector was a bolometer with a silicon chip cooled with liquid helium. The DAC was placed in a

nitrogen gas purged chamber to remove any residual water vapor. The chamber was aligned with a bolometer and the IR beam, in transmission.

The experiments were carried out at the National Synchrotron Light Source on the campus of Brookhaven National Laboratory. The U2A beamline on the Vacuum Ultra-Violet (VUV) ring was used as the IR source. The Bruker microscope collected data in the 550-3500  $cm^{-1}$  range and the bolometer collected spectra within the 100-700  $cm^{-1}$  range. The “white” IR beam passes from the VUV ring into the U2A hutch via a wedged diamond window. The spectrometers had a resolution of 4  $cm^{-1}$ .

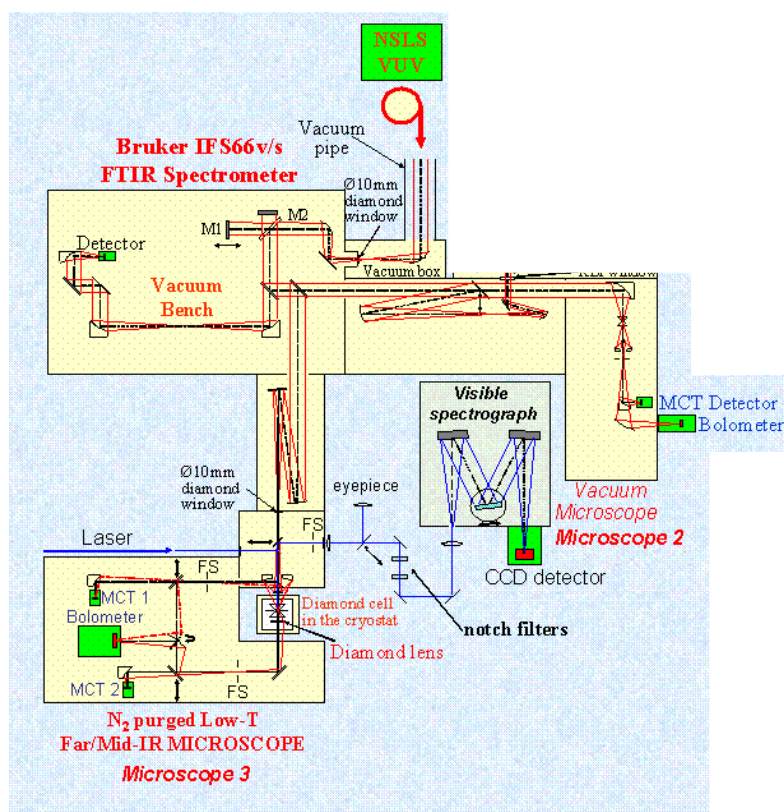


Figure 7: Layout of the interferometer used at the U2A beamlines [19]

## Raman Spectroscopy Experimental Setup

The Raman experiment we performed using a symmetric-style Diamond Anvil Cell (DAC) with two type I low fluorescence diamonds and the culets were roughly 300  $\mu\text{m}$  in diameter. The melamine used was of experimental quality (>99.9%) from Alfa Aesar®. Due to gasket imperfections and to early failure the experiment had to be repeated and resumed at pressures from the terminal pressure of the first experiment. The same melamine sample from the original source was used and the gaskets were both stainless steel. The data does not show any change from either experiment (as expected) so the Raman data is taken from both experiments.

In the first experiment, the gasket was pre-indented to 50  $\mu\text{m}$  thickness and a 120  $\mu\text{m}$  in diameter hole was drilled by an Electric Discharge machine (EDM). Due to the thickness of the pre-indented gasket and the large starting diameter, the gasket failed above 11GPa. A second experiment was then conducted, this time the gasket was pre-indented to 30  $\mu\text{m}$  and the hole was drilled to 90  $\mu\text{m}$  in diameter. This gasket survived to the desired 20GPa pressure. In both Raman experiments, the melamine was ground in a mortar and pestle and packed into the gasket hole with a thermally relieved ruby sphere for pressure determination without the use of a pressure transmitting medium.

There were three acquisitions taken, each was 10 minutes and taken over three different spectral regions to capture all of the vibrational modes discovered from the IR experiments. The grating of the spectrometer was set to were 534 nm, 565 nm, and 615 nm to examine the wavenumbers 83-1365  $\text{cm}^{-1}$ , 1173-2291  $\text{cm}^{-1}$ , and 2700-3600  $\text{cm}^{-1}$  respectively.

The Raman spectral signal to noise ratio is not as good as it was for the IR data; which resulted in several peaks disappearing into the background where the IR data still showed existing peaks. This mostly caused a greater peak uncertainty at higher pressures but the main analysis of the data was unaffected. The plots in Figures 9, 19, and 21 present Raman spectra stacked in order of increasing pressure and show, among other things, the decreasing intensities of the peaks as pressure increases and changes to the spectral pattern.

### X-Ray Diffraction Setup

The X-ray diffraction experiment was performed at HP-CAT in APS on the ID-B beamline. The photons were hard x-rays at  $0.408\text{\AA}$  and the data was collected on a MAR 345 image plate. The symmetric style DAC used for the XRD experiment was the same one used for the Raman and infrared experiments. A stainless steel gasket was pre-indented to a  $50\ \mu\text{m}$  thickness using  $300\ \mu\text{m}$  diameter culets. An EDM was used to drill a  $120\ \mu\text{m}$  diameter hole in the gasket. To achieve a smaller grain size for a better quality powder pattern on the XRD image plate the melamine was ground with a mortar and pestle for 10 minutes. Two ruby spheres were placed on opposite sides of the sample chamber to better determine the sample and the melamine was packed into the rest of the chamber without a hydrostatic medium. The DAC was sealed and the XRD experiments commenced.



## CHAPTER 3

### RESULTS AND DISCUSSION

#### Low Wavenumber

Figure 8 displays stacked far-IR spectral plots with pressure and Figure 9 is of the stacked spectral plots of low wavenumber Raman. The figure does not show any obvious phase transitions at pressures below 14 GPa. However; the plots show the disappearance of low wavenumber peaks above 14 GPa. To best observe where the phase transitions occur we follow the peak positions and watch for any sudden changes in either location or rate of movement. Figures 11 and 12 represent fitted peak positions of far-ir for selected vibrations with pressure. Few peaks in the far-IR region have been identified [26 – 27], making it difficult to understand exactly which bonds are being affected, however; the peak observed near  $160\text{ cm}^{-1}$  appears to correlate with the peak reported by He et al. [21] near 3.96 THz ( $132\text{ cm}^{-1}$ ).

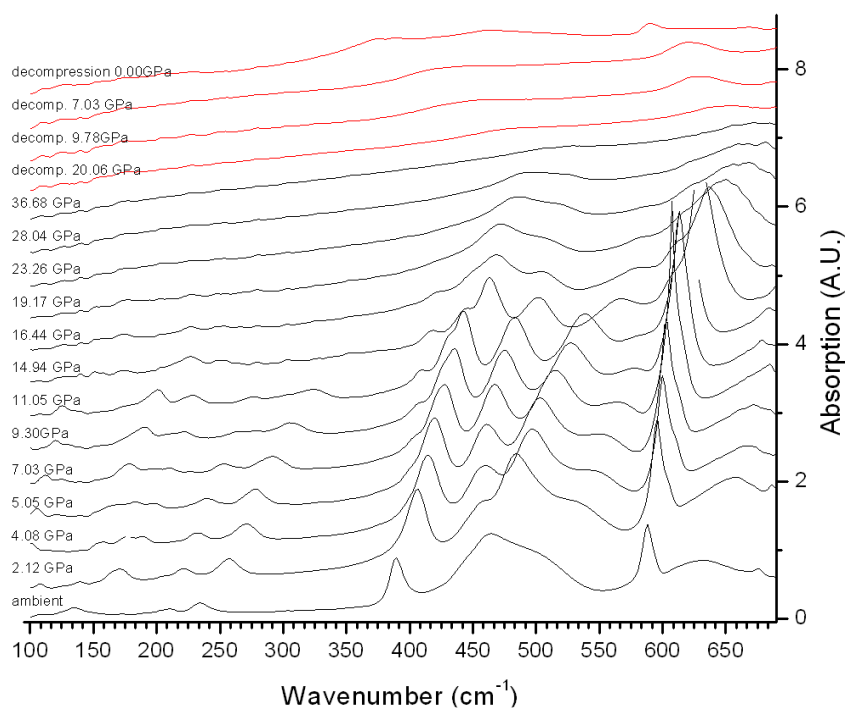


Figure 8: Stacked plot of the far-IR spectra from 0 to 36 GPa. Spectra in black were taken as the sample was compressed; red spectra were collected during sample decompression. A.U. in the y-axis stands for arbitrary units.

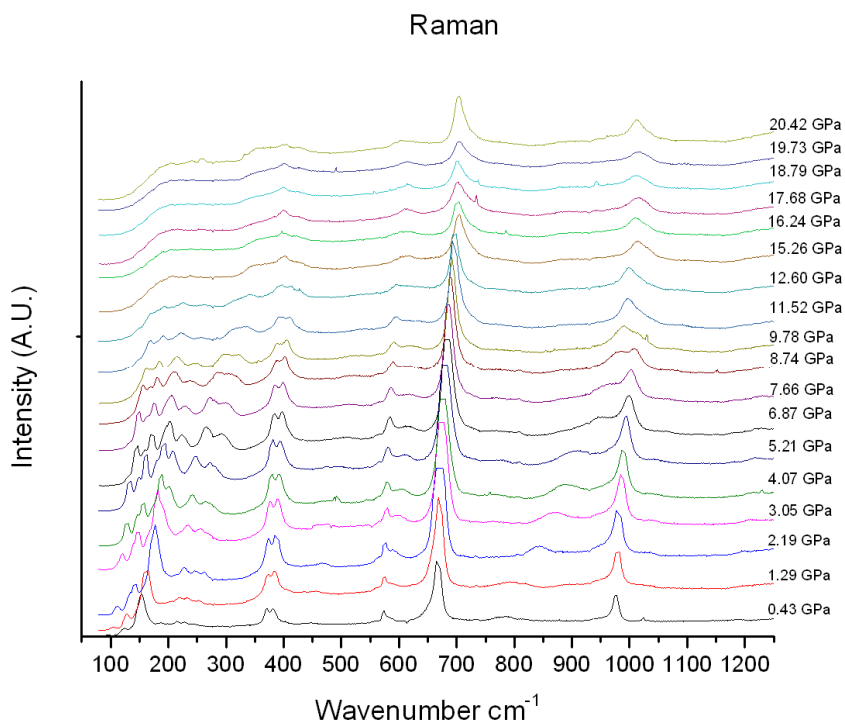


Figure 9: Low wavenumber Raman spectra

A new peak appears at  $170\text{ cm}^{-1}$  at 2.12 GPa, which indicates a phase change coinciding with an observed crystallographic phase change using XRD, which is explained later. Between 2 and 3 GPa, there is a change in the slope of various peak positions as observed in Figures 10 & 11. For the low wavenumber Raman data, there are also several trend line discontinuities as well as new peaks that develop between 2 and 3 GPa which gives further credence to the phase transition at this pressure region. The movement of peaks at  $141$  and  $175\text{ cm}^{-1}$  exhibit trend line discontinuity behavior and can be viewed in Figure 12. The most evident example is the peak at  $780\text{ cm}^{-1}$  as it has a dramatic trend line discontinuity as seen in Figure 13. Along with the change in trendline movement there is a new peak developing near  $131\text{ cm}^{-1}$ . Our IR, Raman, and XRD data all show evidence of a phase transition between 2 and 3 GPa.

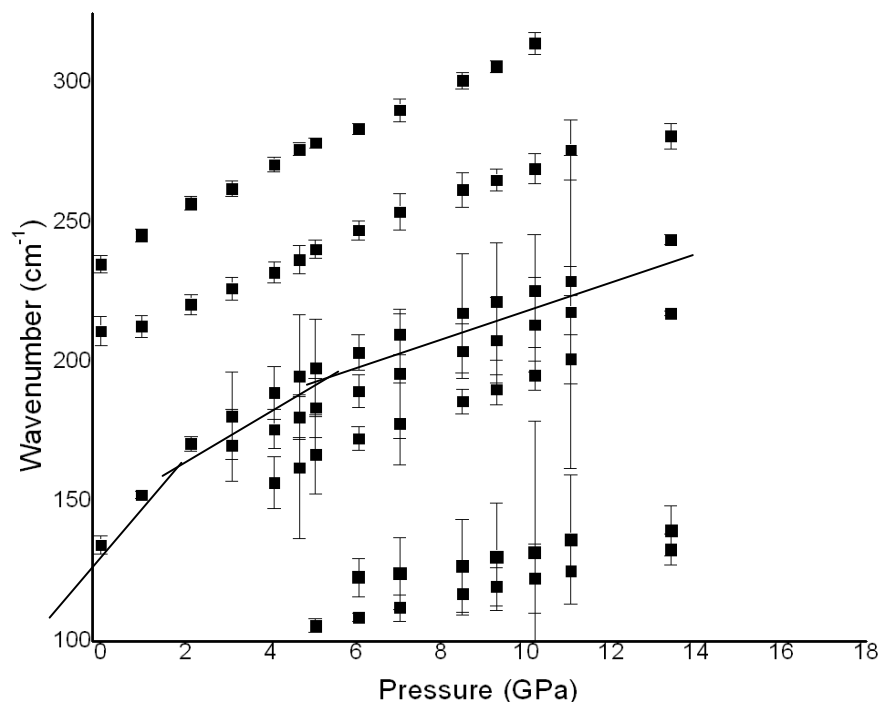


Figure 10: IR peak movement due to increasing pressure in the  $100\text{-}300\text{ cm}^{-1}$  range.

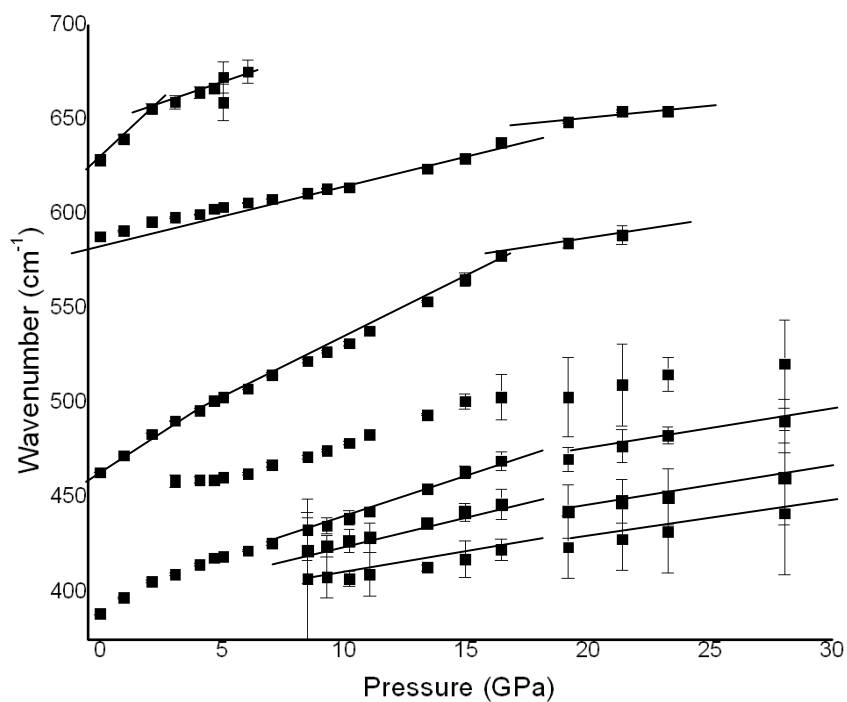


Figure 11: IR peak movement due to increasing pressure in the  $380\text{--}685\text{ cm}^{-1}$  range.

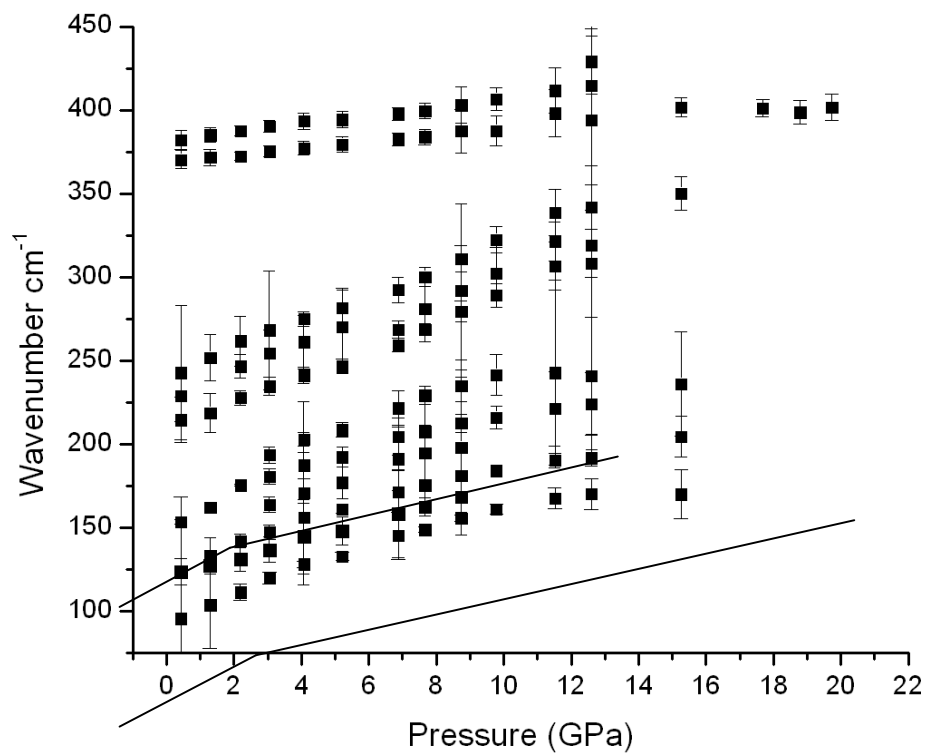


Figure 12: Peak position of low wavenumber Raman spectra

There is believed to be another phase transition near 8 GPa [22-23]. The far-IR data supports this as two new peaks appear near 400 and 425  $cm^{-1}$  between 7 and 9 GPa. The suspected phase change at 8 GPa is still very subtle and the only peak which supports the idea of a phase transition at 8 GPa is near 987  $cm^{-1}$  (Figure 13). The peak significantly shifts toward higher energy between 2 and 8 GPa, and then abruptly levels off at 9 GPa and higher as shown in Figure 13.

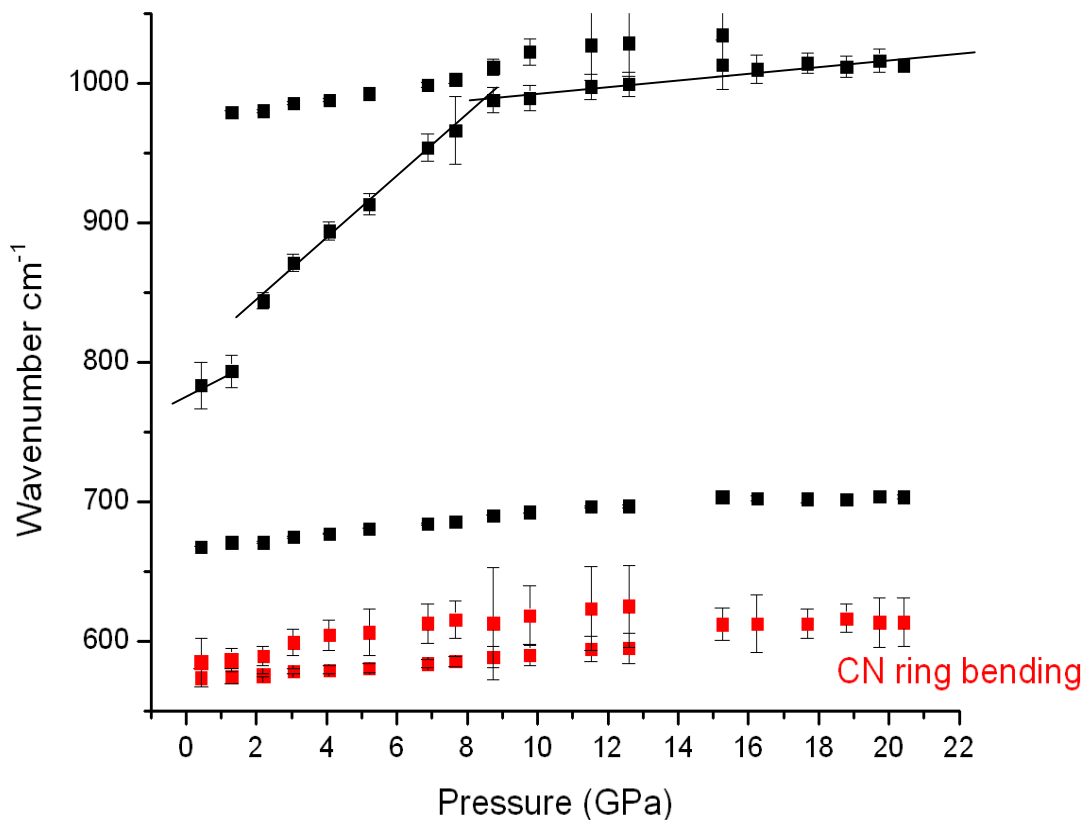


Figure 13: Raman spectra peak position for C-N bonds

In Figure 9 as pressure is increased, all peaks gradually broaden, shifting toward higher frequencies and diminish in intensity as expected. These peaks also exhibit an increase in background. The increase in background would normally be attributed to just

an increase in pressure, as is often seen in high pressure studies. In this case, however, there is a sudden loss of low energy peaks in both the Raman and far-IR spectra, coupled with a dramatic change in the diffraction pattern. With all three of our experiments showing the same effect, we believe this may be an unreported phase transition. In the far-IR data, between 14.9 and 16.4 GPa, five IR peaks disappear between 130 and 320  $cm^{-1}$  (Figure 10). Within the remaining far-ir region (400-600  $cm^{-1}$ ), all peaks appear to experience a slope discontinuity, further supporting evidence of a phase transition. In the Raman data the low wavenumber peaks ( $<350\text{ }cm^{-1}$ ) all vanish above 14 GPa. The x-ray pattern in Figure 26 displays a dramatic change in crystal structure between 11 and 16 GPa. There is at least one new peak and the disappearance of several other peaks. This coupled with the IR and Raman data is strong evidence of a phase transition between 11 and 16 GPa.

#### Mid Range Wavenumber

The mid range modes have been theoretically calculated and can be used to assign which vibrations [26]. The symmetry point group table (Table. 2) for the  $D_{3h}$  group displays the irreducible representations that symmetry affect for IR studies;  $A'_1$ ,  $E'$ , and  $E''$ . The active Raman modes are comprised of  $A'_1$ ,  $E'$ , and  $E''$  [19]. Melamine has a crystal structure possessing eight hydrogen bonding pairs [24]. Although understanding which peaks correspond to hydrogen bonds compared to other bonds is not known. Strong inter-molecular interactions make calculating solid state peaks difficult. This decreases the certainty of whether or not a theoretically calculated mode is truly representing the observed vibration. With these issues in mind, I have matched the theoretical and experimental peaks for both IR and Raman spectra as best as possible. There are a few

vibrations which should be IR inactive and instead appear in the IR spectra and the same issues are seen in the Raman activity. This is understood to be a result of the hydrogen bonding which change the interaction potentials of the system dramatically, ultimately altering the vibration activity in the molecule [25]. Based on this knowledge and the work from reference [26], the mid-IR peaks of melamine have been determined and are presented in Table 3. The presumed peaks between 1000 and 2000  $cm^{-1}$  are predominantly C-N ring based, and can be more easily visualized in Figures 14, 15, and 16 [28-29].

Theoretical ( $cm^{-1}$ ) [26]	Infrared Experimental( $cm^{-1}$ )	Raman Experimental ( $cm^{-1}$ )	Vibration Type	
3464	3469	3464	NH <sub>2</sub> Stretching	E'
3416	3415	3411	NH <sub>2</sub> Stretching	E'
3320	3333	3325	NH <sub>2</sub> Stretching	E'
3125 [27]	3127	3116	Symmetric NH <sub>2</sub>	
1660	1663		NH <sub>2</sub> Bending	E'
1643			NH <sub>2</sub> Bending	E'
1626			NH <sub>2</sub> Bending	E'
1565		1567	Ring stretching (C-N)	E'
1546	1558	1547	Side-chain antisymmetric	
1531		1528	Side-chain antisymmetric	E'
1469		1453	Side-chain CN breathing	A' <sub>1</sub>
1434	1432	1434	Ring stretching (C-N)	E'
1190	1193		NH <sub>2</sub> Rocking	E'
1175			NH <sub>2</sub> Rocking	E'
1022	1031		Ring breathing CN	A' <sub>1</sub>
813	816		Ring bending CN	E'
760			Side-chain out-of-plane CN bend	A'' <sub>2</sub>
730			Ring Bending CN	A'' <sub>2</sub>
619			NH <sub>2</sub> Wagging	A'' <sub>2</sub>
581	587	584	Ring bending	A' <sub>1</sub>
518			Side-chain in-plane CN bending	E'

Table 3: The compilation of theoretical, infrared, and Raman vibration peak wavenumbers. Blank sections are either due to the mode being inactive or the error proved too great to include the peak.



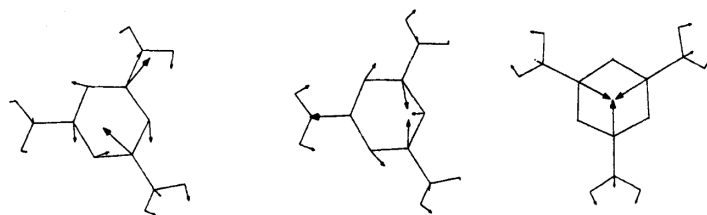


Figure 14: Eigenvectors of the calculated modes in the range  $1450\text{-}1500\text{ cm}^{-1}$ . Starting from left to right these vibrations are predicted to be  $1485$ ,  $1485$ , and  $1461\text{ cm}^{-1}$  [26]

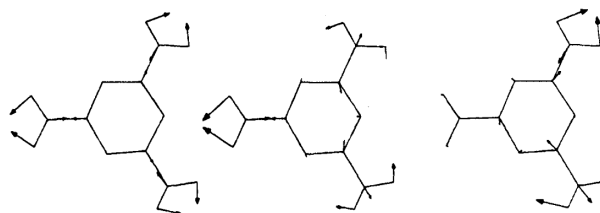


Figure 15: Calculated vibrational modes from left to right,  $1599$ ,  $1592$ , and  $1591\text{ cm}^{-1}$  [26]

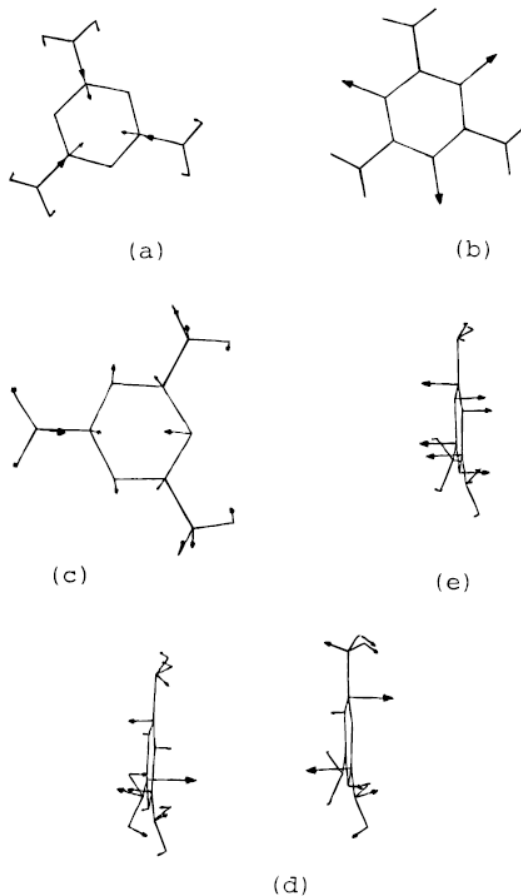


Figure 16: Eigenvectors of calculated modes between  $600\text{-}1000\text{ cm}^{-1}$ . a.)  $645\text{ cm}^{-1}$  b.)  $966\text{ cm}^{-1}$  c.)  $578\text{ cm}^{-1}$  d.)  $674\text{ cm}^{-1}$  e.)  $830\text{ cm}^{-1}$  [25]

Examining the mid-IR stacked plot (Figure 17) gave no obvious signs of any phase transitions. There are no new peaks or otherwise dramatic changes in the spectra between 1000 and 2000  $cm^{-1}$ . The peak positions increase smoothly with pressure showing no signs of a phase transition (Figure 18). At the pressures of the first two phase transitions, (2-3 GPa and 8 GPa) the Raman shows little change either visually (Figure 19) or with peak position (Figure 20). With both types of vibrational spectroscopy passing two previously determined phase transitions without any noticeable change leads to a possible conclusion which is complemented by the work of X.R. Liu et al [30]. Their results state that the peaks increase in wavenumber monotonically and with no indication of a phase transition at either 2 or 8 GPa. The mid range wavenumber peaks are predicted to consist of ring based (C-N) vibrations [26]. Therefore, the consistent movement of the peaks implies that the s-triazine ring is most likely unaffected by the structural transitions with its unit cell as was also concluded by the work of X.R. Liu[30].

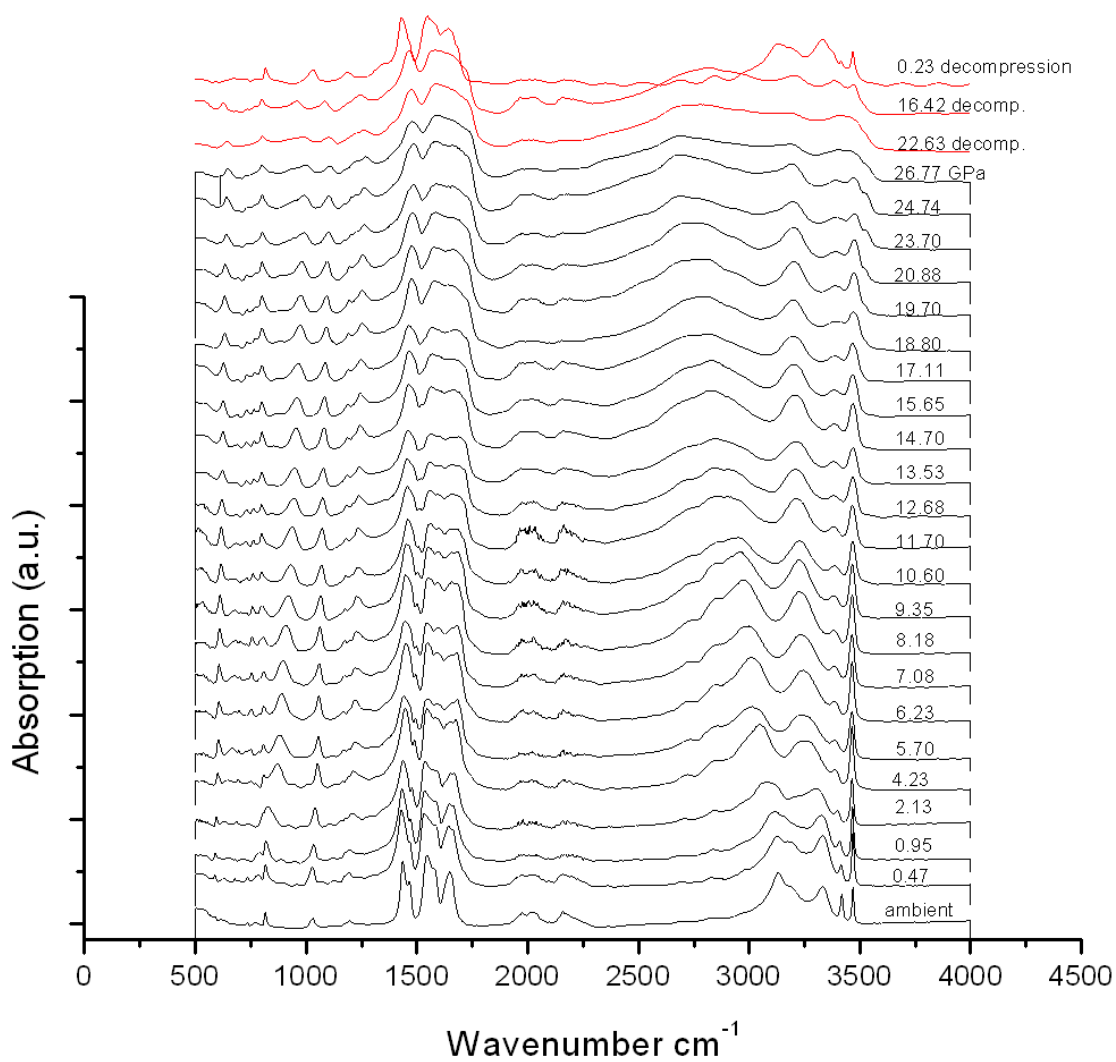


Figure 17: Stacked plot of mid-IR spectra. Black represents increasing pressure, while red is decreasing pressure. The wavenumber region between  $1800 - 2500 \text{ cm}^{-1}$  is heavily influenced by diamond absorption and are therefore not used in our data analysis.

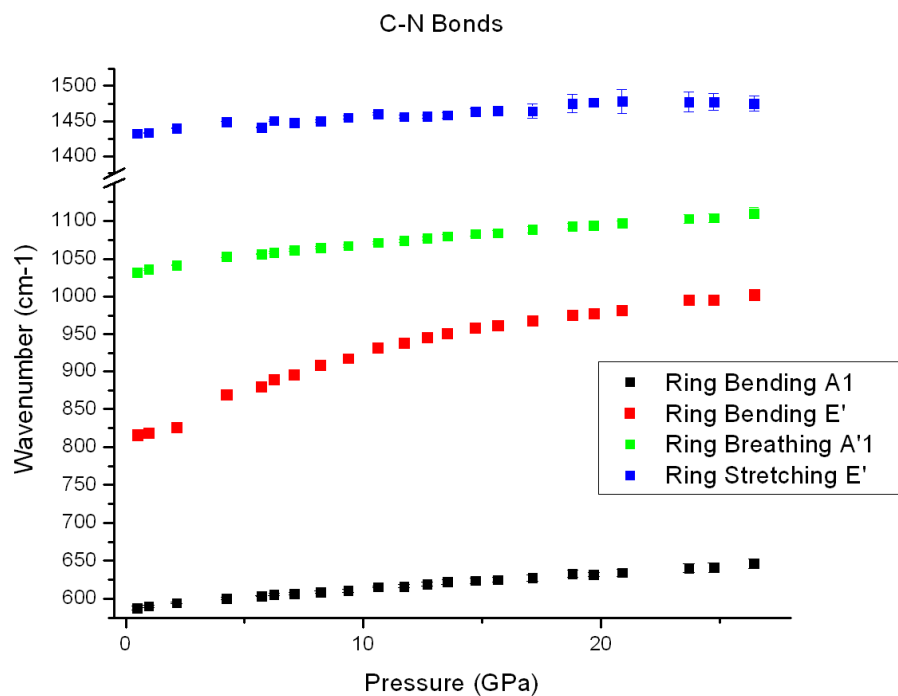


Figure 18: The IR carbon-nitrogen ring bonds peak position with increasing pressure

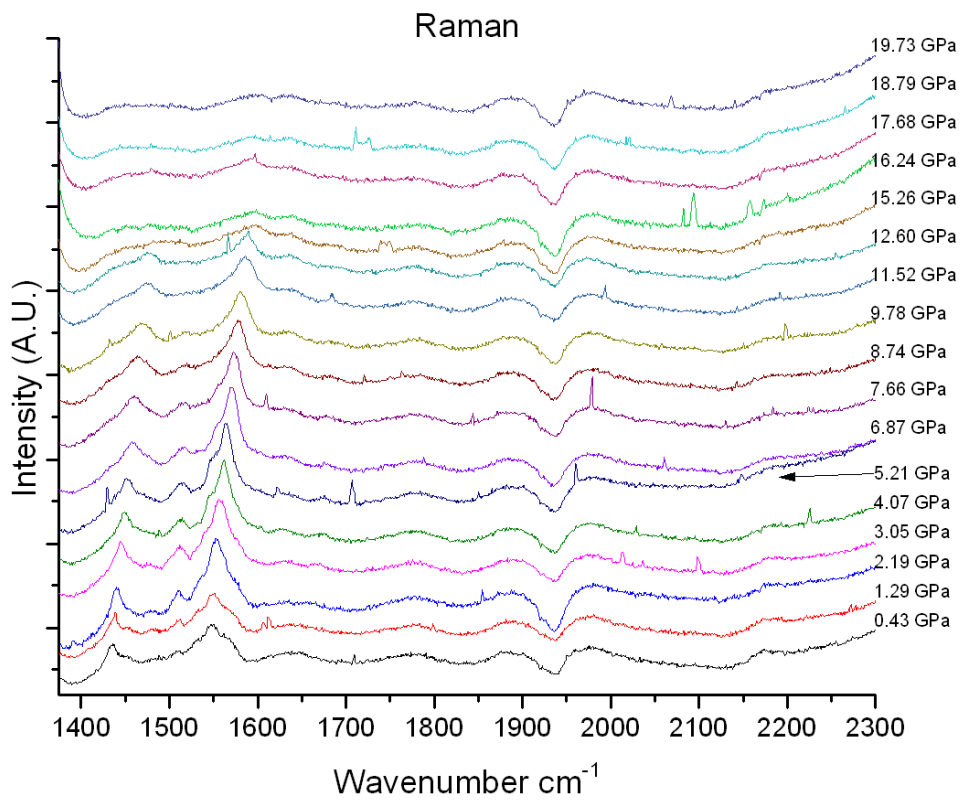


Figure 19: Mid Range wavenumber Raman spectra

There is a significant trend line change in the 1528 and 1547  $cm^{-1}$  Raman peaks with pressure after 14 GPa, which coincides with the pressure of the unreported phase transition (Figure 20). This is the only evidence of the 14 GPa phase transition when observing the mid range IR or Raman.

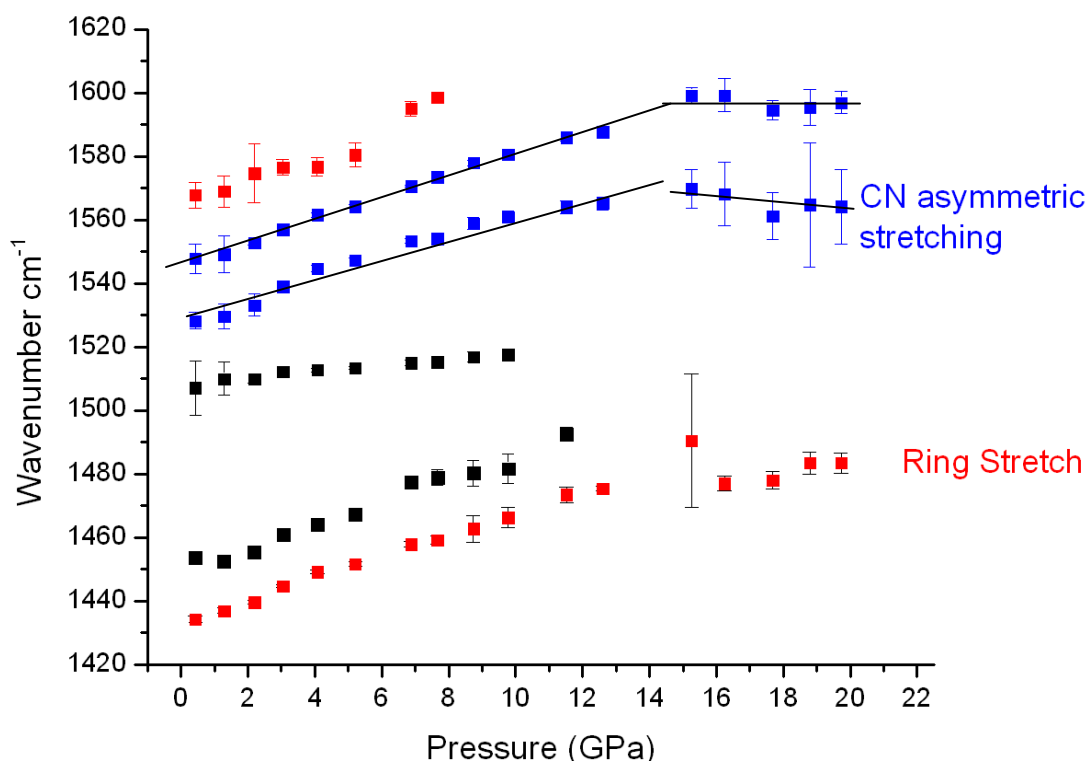


Figure 20: Raman spectra peak position for ring C-N bonds

#### High Wavenumber Studies in the 2800-3600 $cm^{-1}$ Range

There are four anomalous peaks which weaken as pressure increases. These peaks are observed in both types of experiments and they behave identically. Figure 21 shows a stacked plot of the high wavenumber Raman experiment and the movement of the peaks becomes evident. The two most obvious modes are identifiable to vibrations near 3125 and 3333  $cm^{-1}$  for IR and 3116 and 3325  $cm^{-1}$  for Raman, (see Figures 22 and

23). Both vibrations decrease in energy dramatically with pressure. The other two 3000  $cm^{-1}$  modes observed in the IR and Raman studies decrease in energy, but only slightly. Regardless, all high wavenumber  $NH_2$  peaks show a decrease in wavenumber.

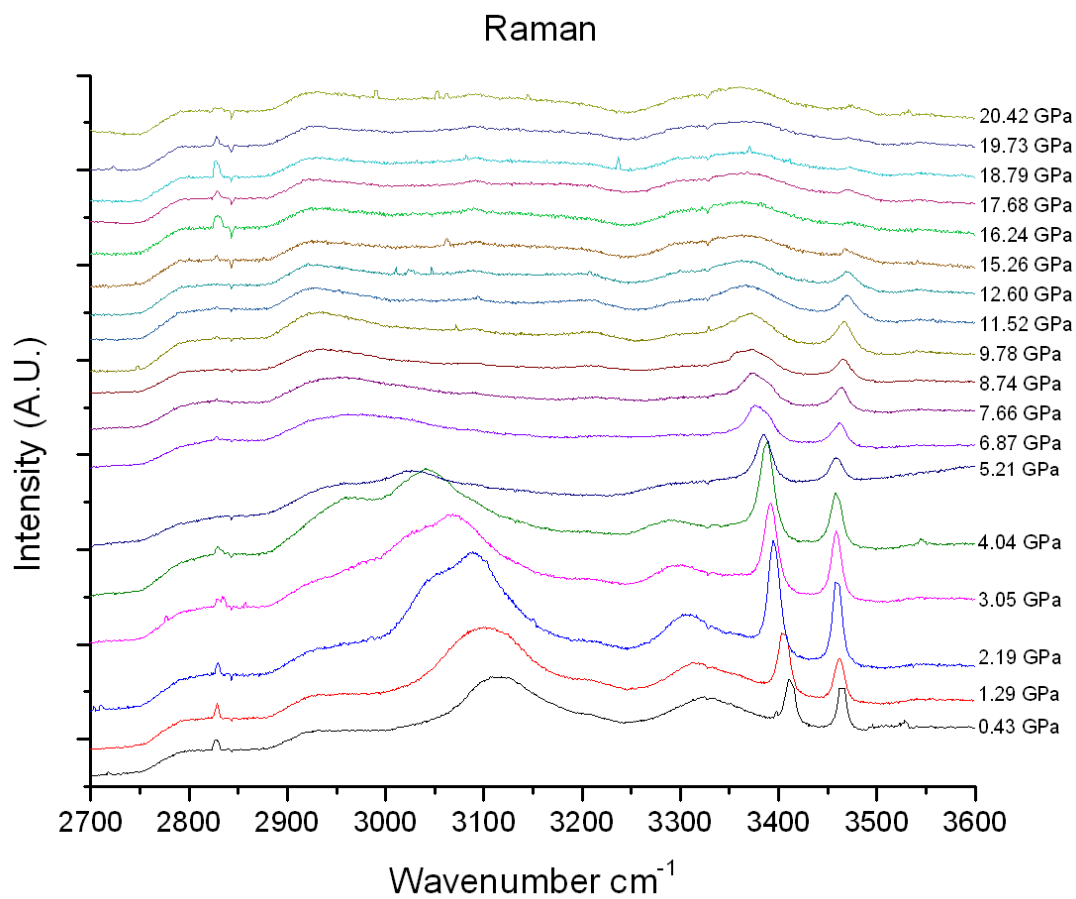


Figure 21: Stacked high wavenumber Raman spectra.

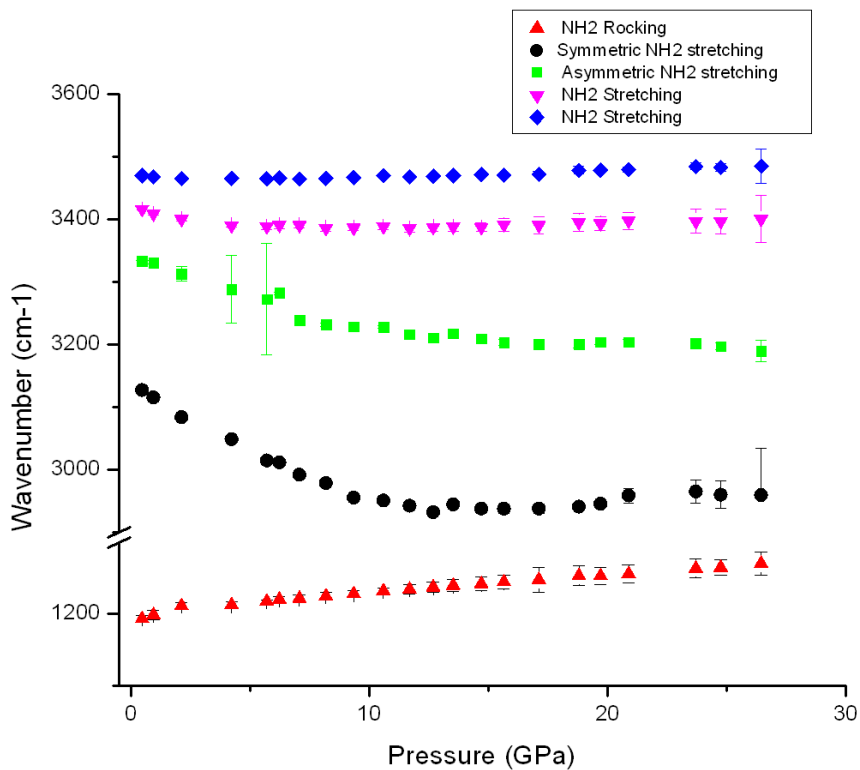


Figure 22: IR peak positions of the manifold of NH<sub>2</sub> vibrations as pressure is increased.

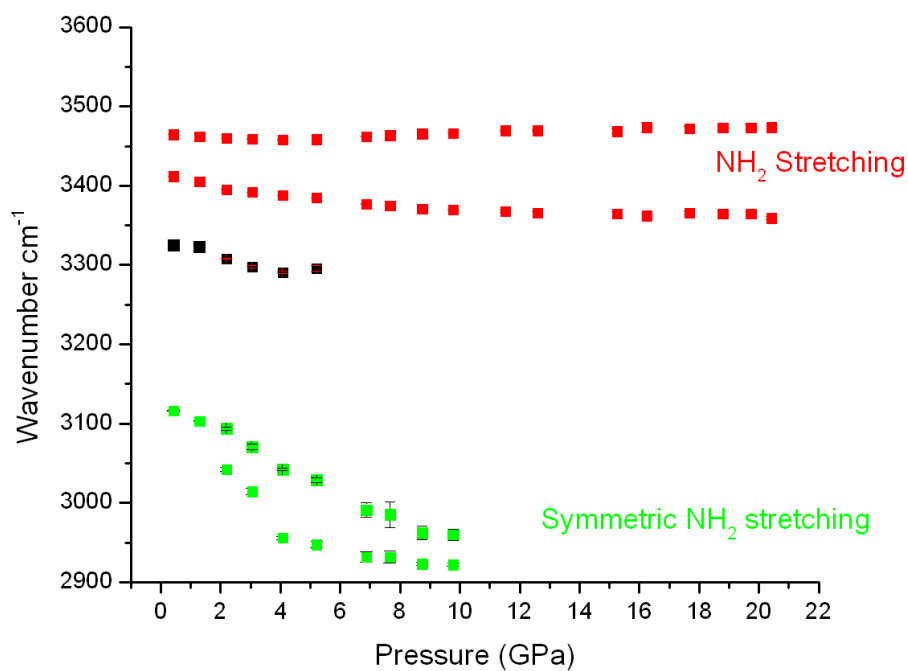


Figure 23: Raman spectra peak position for N-H and hydrogen bonding related modes.

This suggests that as the molecules are brought closer, hydrogen bonding increases. The intra-molecular N-H bond may weaken due to electronic delocalization towards neighboring molecules, implying a shift in electron density [23,30]. The bonds that weaken are the  $NH_2$  symmetric and antisymmetric stretching bonds, and such behavior was also observed in TATB [23]. The decrease in IR wavenumber continues until 15 GPa, where it remains roughly constant or slightly increases. This further corroborates our far-IR evidence of a possible phase transition at the same pressure. The peak positions of the high frequency mid-IR vibrations associated with the  $NH_2$  group can be observed in Figure 22. The 3116 and 3325  $cm^{-1}$  lines followed a similar path except that they were lost in the background after 10 GPa. This would imply that the phase transitions are mainly affecting amine branches. The Raman plot containing the ring vibrations shows the same behavior (see Figure 18), thus giving further credence towards X.R. Liu's claim [30].

#### X-Ray Diffraction

Upon examining the XRD data, the argument for the phase transitions claimed in the IR and Raman gains even more strength. H.A. Ma et al. [22] as well as M. Pravica et al. [23] suspect that there is a phase transition between 1 and 2 GPa. The XRD pattern in Figure 24 contains two new peaks emerging between 2 and 3GPa. The difference in pressure between the work of H.A. Ma et al. and our own may be attributed to an uncertainty with pressure since our experiments did not have a hydrostatic medium.



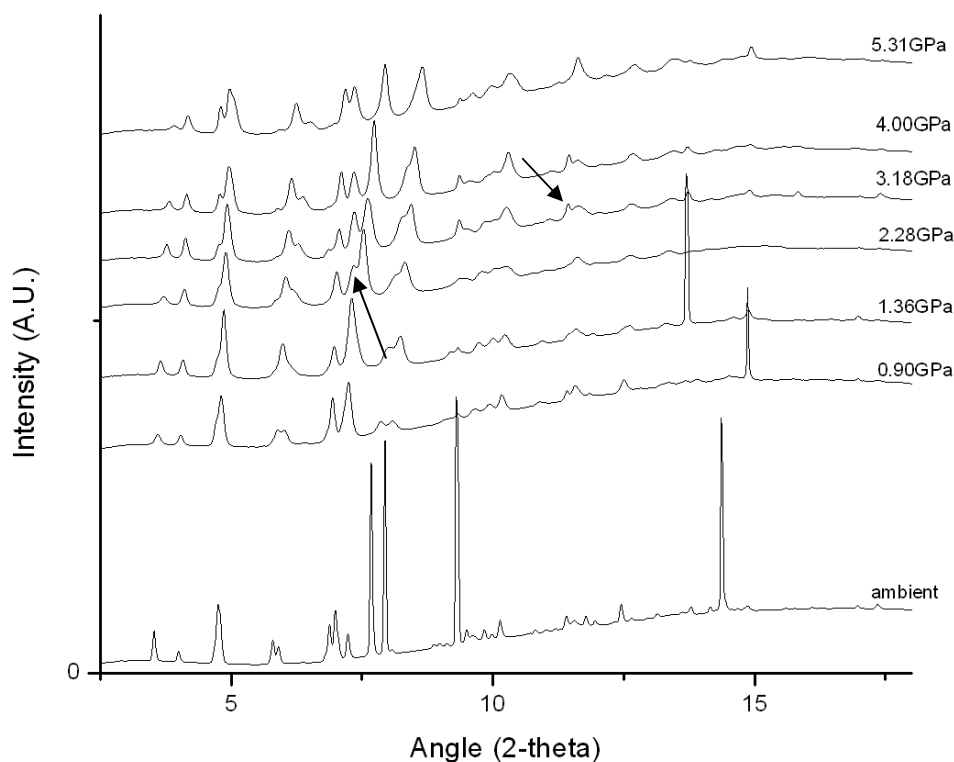


Figure 24: X-ray diffraction showing the first phase transition. The arrows indicate the peaks which have a notable change and give evidence of a phase transition.

The crystal structure of melamine is reported to change from triclinic to orthorhombic between 7 & 9 GPa [22]. At the suspected pressure the pattern simplifies with the merging of two peaks and the loss of another (Figure 25). What appears as the simplification of the melamine unit cell lattice structure would agree with the conclusion that the structure is transitioning to a more ordered formation. There is no mention of this in previously published x-ray studies, whereas the Raman paper by X.R. Liu et. al. suggests that the peaks were lost due to high pressure broadening. The IR and Raman data did not show any changes peak movement however, new peaks appeared in both spectra between 7 and 8 GPa to further support our claim of a phase transition. The most notable change in the XRD pattern is seen between 11 and 16 GPa. The dramatic change

in the crystal structure is evident as several peaks disappear (Figure 26), coinciding with concomitant changes in the IR and Raman data. The far-IR and low wavenumber Raman data show a loss in most peaks at this transition which could imply a loss in the intermolecular activity resulting in a change in the unit cell structure of melamine and or sample amorphization.

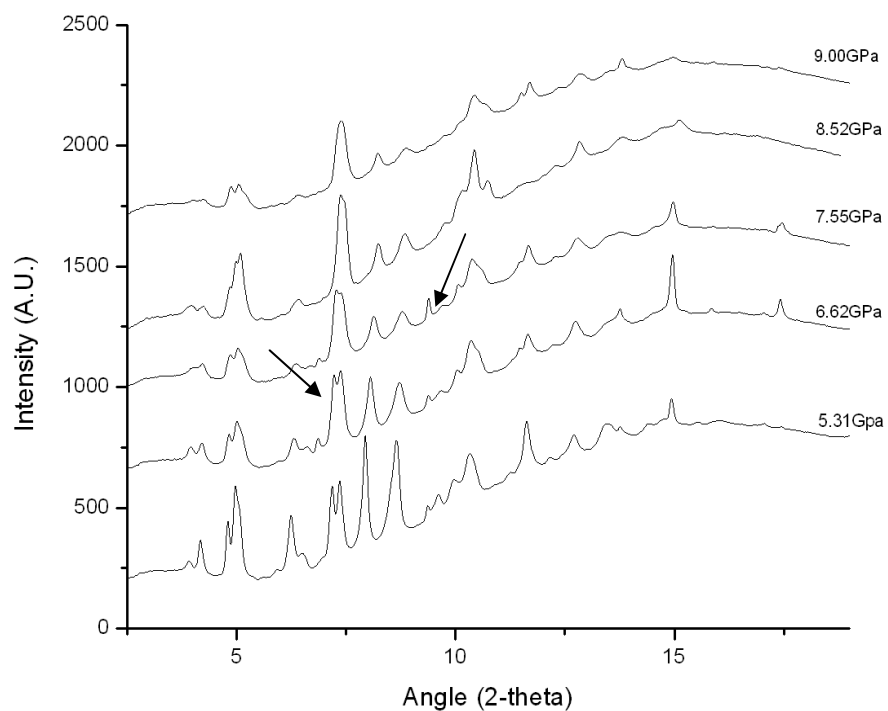


Figure 25: XRD of the second phase transition. The merging peaks and disappearance of a peak (both are labeled with arrows) give credence to the phase transition near 8 GPa.

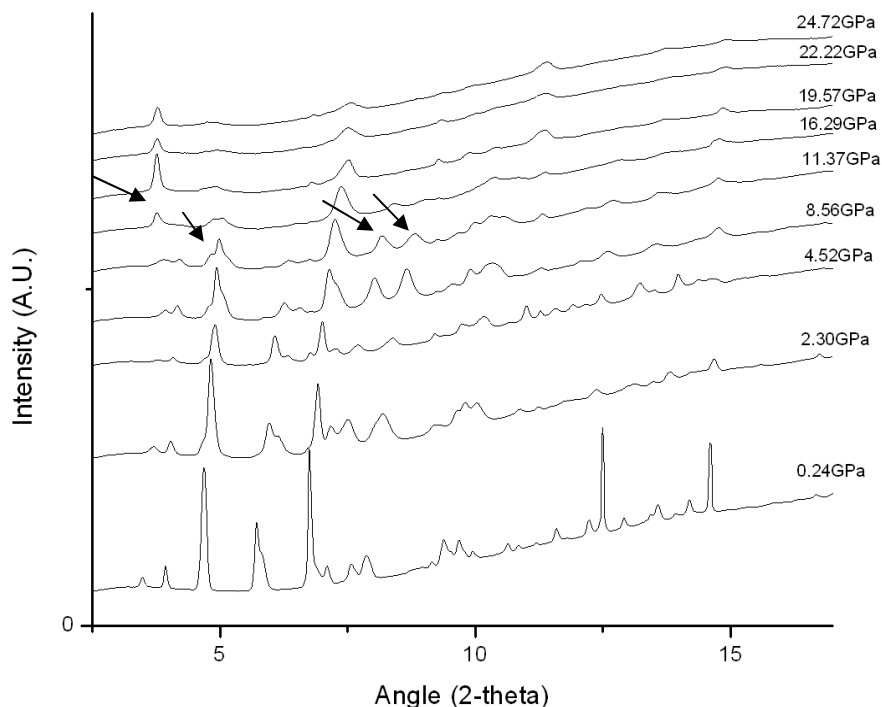


Figure 26: XRD showing the phase transition around 16 GPa. There are several changes between 11 and 16 GPa, some peaks disappear while at least one peak appears.

### Decompression

The IR and Raman decompression spectra were taken immediately after achieving the highest pressure of this study (36 GPa). The decrease and eventual disappearance of the low wavenumber peaks may imply that the crystal structure may be permanently disordered and/or amorphous. The IR peaks below  $388\text{ cm}^{-1}$  (Figure 8) and the Raman peaks below  $300\text{ cm}^{-1}$  (Figure 27) did not appear to return even at ambient pressure. The few peaks that did return are very broad and have a lowered intensity. When examining the decompressed XRD data (Figure 28) none of the Bragg peaks returned to their former  $2\theta$  positions. This gives reliable evidence of melamine's inability to recover long range molecular interactions to below 20 GPa.

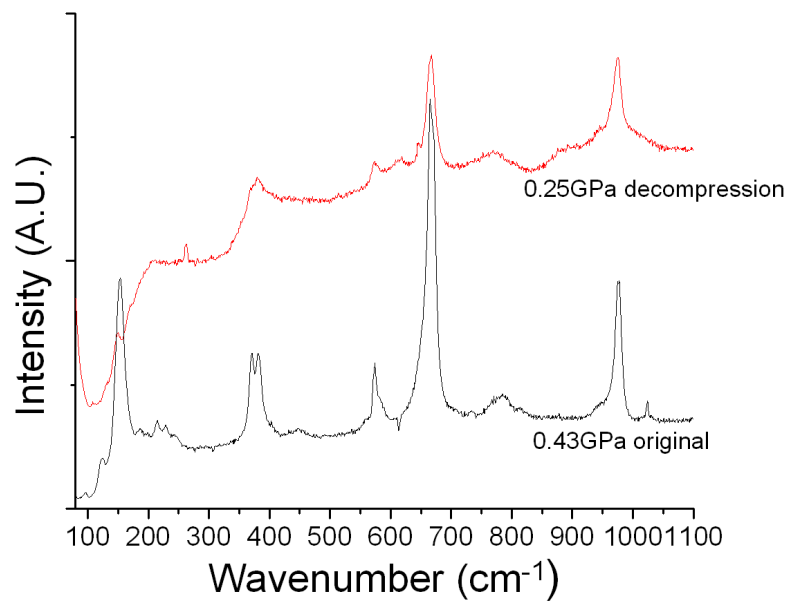


Figure 27: Raman decompression for low wavenumbers

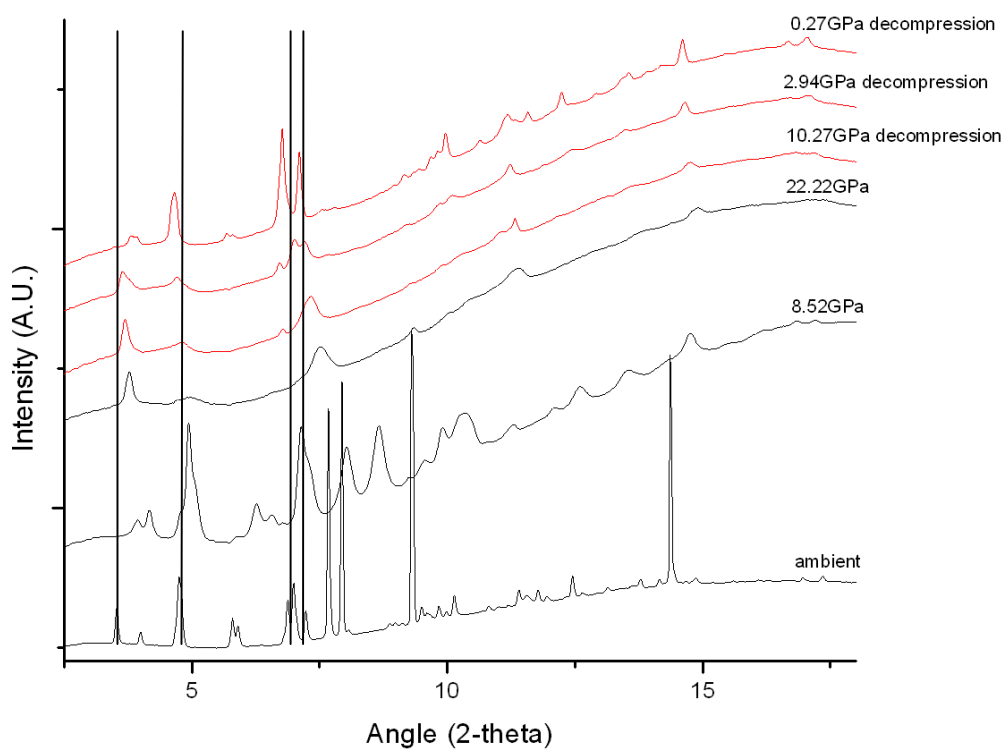


Figure 28: Decompression XRD. The melamine does not appear to return to its original phase upon returning to ambient pressure.

Melamine appears to suffer no permanent intra-molecular damage from pressure cycling. The spectral patterns appear fully reversible as the Figures 29 & 30 illustrate. All symmetric and antisymmetric vibrations also return to their original wavenumber, the black triangle represents the ambient peak position before increasing pressure. The Raman data between 1400-3600  $cm^{-1}$  concurs with similar results of peaks returning to their original wavenumbers, suggested in Figures 31 and 32.

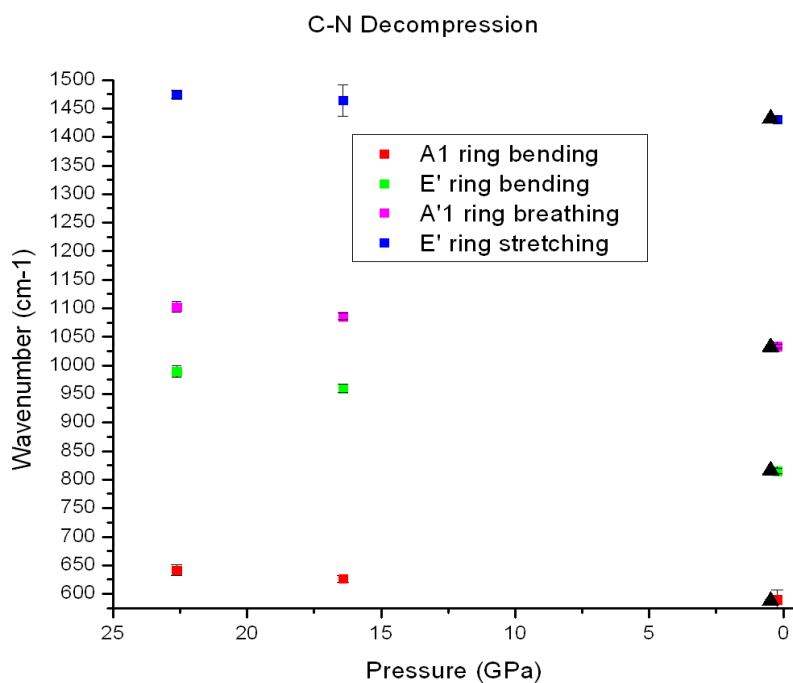


Figure 29: IR, C-N peak positions as a function of decreasing pressure. Note that the black triangles, which represent peak positions at ambient conditions, are very close to the original peak positions.

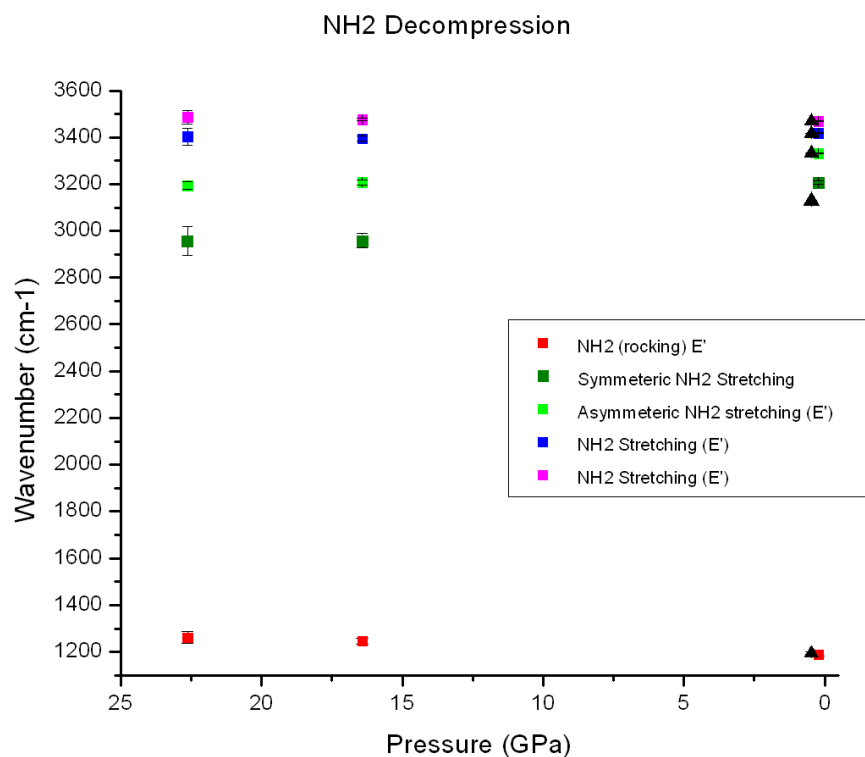


Figure 30: IR peak positions of NH<sub>2</sub> with respect to wavenumber as pressure is reduced.

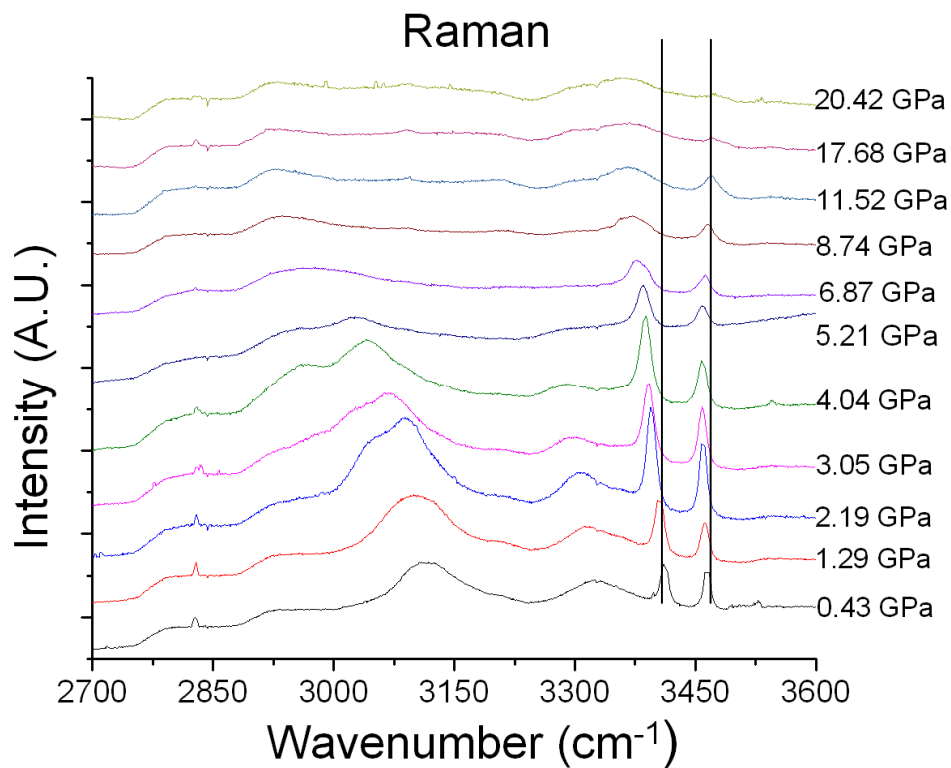


Figure 31: Raman decompression for high wavenumbers

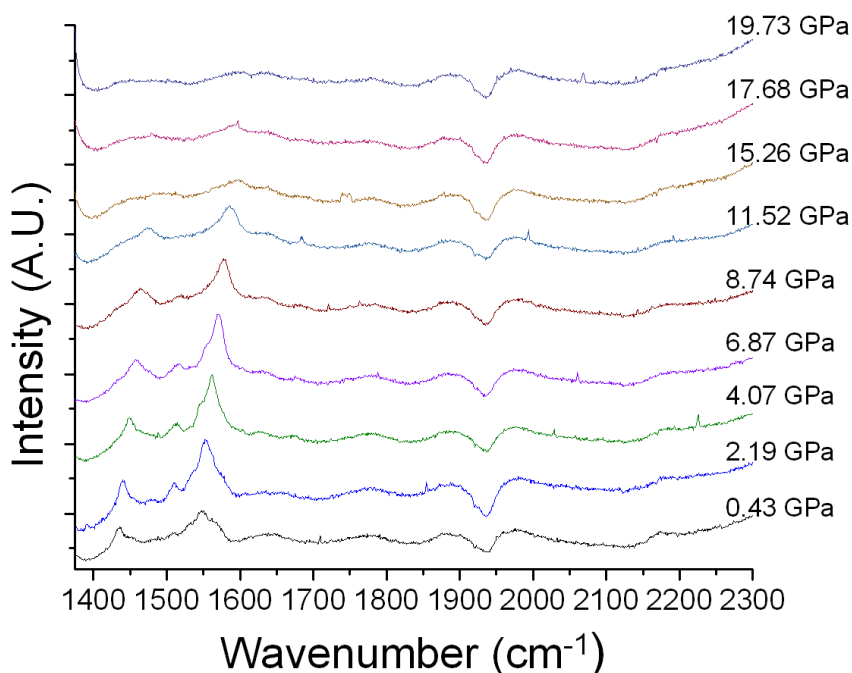


Figure 32: Raman decomposition for mid-range wavenumbers

## CHAPTER 4

### CONCLUSION

We have reported the first far-IR study of melamine at high pressure (to 36 GPa) and have expanded the investigated pressure range of this industrially important molecule in the mid-IR region by a factor of six (to 26 GPa). We have provided evidence consistent with the occurrence of least two phase transitions near 2 and 8 GPa, respectively, which were observed in earlier studies [22-23]. The far-IR and Raman data displayed trend line discontinuities between 2 and 3 GPa. The XRD pattern exhibits new peaks splitting from the previous and new peaks entirely. At 8 GPa, the IR data revealed new peaks which split off from earlier ones, and the diffraction pattern simplified as peaks merged or vanished. We have likely observed an unreported phase transition near 15 GPa for the first time. The mid-IR and Raman experiment demonstrated near

complete reversibility of intra-molecular bonds. The far-IR and Raman experiments suggests irreversible long range interactions with pressure cycling. The most easily detected change for this pressure came from the XRD, showing a dramatic simplification of the crystal structure. This included the loss of several peaks and the addition of a few others; the most notable are denoted with arrows in Figure 26. The symmetric and antisymmetric N-H bonds weaken with pressure which was also observed in TATB [23]. Our studies are useful in that we have examined the behavior of melamine, an industrially important material under extreme conditions which will contribute knowledge pertaining to chemistry of the molecule at high pressure.



## APPENDIX

ANL – Argonne National Laboratory  
APS – Advanced Photon Source  
BNL – Brookhaven National Laboratory  
CCD – Charged Couple Device  
DAC – Diamond Anvil Cell  
EOS – Equation of State  
HP-CAT – High Pressure-Collaborative Access Team  
IR – Infra-Red  
FTIR – Fourier Transform Infra-Red  
GPa – Giga-Pascals  
LANL – Los Alamos National Laboratory  
NSLS – National Synchrotron Light Source  
TATB – Triaminotrinitro Benzene  
UNLV – University of Nevada, Las Vegas  
XRD - X-ray Diffraction

## References

1. S. Trasobares et al. *Journal of Physical Chemistry A*, **107** 228 (2003).
2. M. Pravica, M. Galley, C. Park, H. Ruiz, J. Wojno, *Diamond Related Materials* **20**, pp. 1090-1092 (2011).
3. J. Kemsley, *Chemistry & Engineering News*. 89, pp. 32-34 (2011)  
<http://pubs.acs.org/cen/science/89/8929sci2.html>
4. For example, please see: <http://www.sciencebase.com/science-blog/melamine-in-milk.html>
5. D.M. Teter, R.J. Hemley, *Science*, **53**, 271 (1996).
6. BeamLok 2060 Ion Laser User Manual, Spectra-Physics (1994)
7. Yariv, Amnon. *Quantum Electronics*. 3rd. John Wiley & Sons, Inc., 1988.
8. Ernst-Eckhard Koch. *Handbook on Synchrotron Radiation*, Vol. 1a, North Holland, 1983
9. Kittel, Charles. *Introduction To Solid State Physics*. John Wiley & Sons Inc, 9-31. 2005
10. K. Syassen. *High Pressure Research*, **28**, 75 (2008)
11. Mao, H.K., et al. *Journal of Applied Physics*. **49**, 3276 (1978)
12. G. J. Piermarini, S. Block, J. D. Barnett, and R. A. Forman *Journal of Applied Physics*. **46**, 2774. (1975)
13. Brian Hosterman *Raman Spectroscopic Study of Solid Solution Spinel Oxides*. Ph.D. Dissertation. University of Nevada, Las Vegas August 2011
14. Olver, Frank W. J. Olver, and National Institute of Standards and Technology (U.S.). Ed. *NIST Handbook Of Mathematical Functions*. Cambridge Univ Pr, 2012.
15. Ferraro, O. R., Nakamoto, K., & Brown, C. W. *Introductory Raman Spectroscopy*. (second ed.). (2003).
16. Atkins, E. W., & Paula, J. D. *Physical Chemistry*. W. H. Freeman. (2006).
17. Engel, H., & Reid, P. J. *Physical Chemistry*. Benjamin-Cummings Pub Co. (2006).

18. Griffiths, E. R., & Haseth, J. A. D. *Fourier Transform Infrared Spectrometry*. Wiley-Interscience (1986).
19. Chemical Portal: <http://www.webqc.org/printable-symmetrypointgroup-ctd3h.html>
20. Z. Liu, U2A beamline webpage <http://www.bnl.gov/u2a/setup/index.html>
21. M. He et al. *Chinese Optics Letters*. **9**, S10507-1 to S10507-3 (2011)
22. H.A. Ma et al. *Chemical Physics Letters*. **368**, 668-75 (2003)
23. M. Pravica, B. Yulga, S. Tkachev, and Z. Liu. *Journal of Physical Chemistry. A*, **113** (32): 9133-9137. (2009)
24. S. D. Hamann and M. Linton, *Australian Journal of Chemistry*. **28**, 2567-78 (1975)
25. Ferraro, O. R., & Basile, L. (1978). *Fourier Transform Infrared Spectroscopy, Applications to Chemical Systems*. (Vol. 1). Academic Pr.
26. W. J. Jones and W. J. Orville-Thomas *Transactions for the Faraday Society*. **55**, 203-210 (1959)
27. L. Costa and G. Camino, *Journal of Thermal Analysis*. **34**, 423-239 (1988)
28. Koglin E, Kip B J, and Meier R J 1996 *Journal of Physical Chemistry*. **100** 5078
29. R.J. Meier, J.R. Maple, M.-J. Hwang, and A.T. Hagler *Journal of Physical Chemistry*. **99**, 5445-5456. (1995)
30. X R Liu, P V Zinin, L C Ming, T Acosta, S K Sharma, A K Misra, S M Hong. *Journal of Physics*. **215**, (2010)
31. Microscopy Resource Center  
<http://www.olympusmicro.com/primer/techniques/confocal/laserintro.html>

VITA

Graduate College  
University of Nevada, Las Vegas

Martin D. Galley

Local Address:

1601 East Katie ave. APT 209  
Las Vegas, NV 89119

Degree:

Bachelor of Science, Physics, 2009  
State University of New York College at Cortland, Cortland, NY

Thesis Title: Spectroscopic Studies of Melamine at High Pressure

Thesis Committee:

Chairperson, Dr. Michael Pravica  
Committee Member, Dr. Andrew Cornelius  
Committee Member, Dr. Stephen Lepp  
Graduate Faculty Representative, Dr. Clemens Heske